Nuclear Instruments and Methods in Physics Research A278 (1989) 293–317
North-Holland, Amsterdam

THE BATES POLARIZED ELECTRON SOURCE

G.D. CATES *, V.W. HUGHES, R. MICHAELS, H.R. SCHAEFER and T.J. GAY **
Yale University, New Haven, CT 06520, USA

M.S. LUBELL
City College of the City University of New York, New York, NY 10031, USA

R. WILSON
Harvard University, Cambridge, MA, USA

G.W. DODSON, K.A. DOW, S.B. KOWALSKI and K. ISAKOVICH
Massachusetts Institute of Technology, Cambridge, MA, USA

K.S. KUMAR, M.E. SCHULZE +, P.A. SOUDER and D.H. KIM
Syracuse University, Syracuse, NY, USA

Received 21 December 1988

A polarized electron source, based on photoemission from GaAs, has been developed and installed at the MIT Bates Linear Accelerator Center. A multichamber vacuum system houses up to four GaAs crystals simultaneously, and is contained in a Faraday cage to provide about 300 keV in electrostatic acceleration. A modulated cw krypton ion laser is used to achieve stable operation during 15 μs pulses with a repetition rate of 600 Hz. The source has produced pre-injected peak currents in excess of 17 mA, and accelerated peak currents of 8 mA. The source has a calculated transverse phase space of $10^{-3}\ \pi m_e c - cm$. Developed for initial use in a parity violation measurement in elastic polarized $\vec{e}$–^{12}C scattering, the first beam polarization measurement was 0.36 ± 0.04, as determined by Møller scattering at 250 MeV. Subsequent beam polarization measurements have yielded polarizations as high as 0.40 ± 0.03.

1. Introduction

This paper describes a newly constructed polarized electron source that has been installed at the MIT Bates Linear Accelerator Center. The source employs the technique of photoemission from GaAs [1–3], and is substantially different from earlier sources based on the same technique [4–6]. Polarized electrons open a new dimension in the field of electron scattering at medium energies. Inclusive scattering, coincidence measurements, and experiments in which the nuclear target is also polarized are examples of the wide spectrum of nuclear physics measurements that can take advantage of polarized electrons. The breadth of physics to be learned includes the fundamental electro-weak interaction of electrons with nuclear currents, the structure of nucleons, nuclear resonances, the behavior of few-body systems, and the isolation of various multipole amplitudes in scattering from complex nuclei. High energy physics has benefited richly from the use of polarized electrons [7–11]; the benefit to nuclear physics appears just as great.

The strength of polarization measurements lies in their ability to isolate important but small amplitudes in scattering processes that otherwise would be masked by the more dominant amplitudes. There are two reasons for this, one theoretical and one experimental. For unpolarized scattering where the spins are averaged, the observed cross section typically depends upon the sums of squares of amplitudes. When spin dependence is included, however, new terms in the cross section arise

* Present address: Department of Physics, Princeton University, Princeton, NJ 08544, USA.
** Present address: Department of Physics, University of Missouri-Rolla, Rolla, MO 65401, USA.
+ Present address: Science Applications International Corp., Princeton, NJ 08540, USA.

0168-9002/89/$03.50

which are bilinear products of different amplitudes. An important case for polarized scattering is where a small amplitude of interest is multiplied by a large amplitude, greatly enhancing its effect. The experimental advantage is that the direction of the polarization of the beam may be changed rapidly without appreciably changing any other experimental parameter such as geometrical acceptance or counter efficiency. Thus the spin dependent part of the cross section can be extracted with minimal systematic errors.

Examples of small amplitudes that at present are poorly known and which may be measured best with polarized electrons include G_E for the neutron [12–15] and the C2 amplitude in production of the Δ-resonance [16,17]. We note that some of the proposed experiments to measure G_E are experiments in which both the incident electrons and the nuclear target are polarized [14,15]. Also, coincidence experiments using polarized electrons have been proposed in which a nucleon is detected out of the scattering plane [18,19]. The out of plane coincidence measurements facilitate the determination of structure functions that otherwise are averaged over without the use of polarized electrons [20].

The original motivation for the development of the polarized electron source at the Bates accelerator, however, was the study of the effect of weak neutral currents in elastic scattering from ^{12}C [21–23]. The experiment determines the parity nonconserving asymmetry

$$A_{PNC} = \frac{\sigma_R - \sigma_L}{\sigma_R + \sigma_L}, \tag{1}$$

where σ_R (σ_L) is the cross section for scattering right (left) handed electrons. In the standard model, the magnitude of the effect can be written in terms of the momentum transfer Q, the proton mass M_p, and the weak mixing (Weinberg) angle θ_W according to the expression [24]

$$A_{PNC} = 3.17 \times 10^{-4} \frac{|Q|^2}{M_p^2} \sin^2\theta_W. \tag{2}$$

At a value of $Q = 150$ MeV/c, corresponding to an elastic scattering energy of 250 MeV and a laboratory scattering angle of 35° for a fixed target, eq. (2) predicts the asymmetry to be $\sim 10^{-6}$. Although clearly difficult to measure, A_{PNC} nonetheless is six orders of magnitude larger than the actual contribution of the weak interaction to the unpolarized cross section. It is the rapid reversal of the beam helicity under well controlled optical conditions, however, that ultimately makes the measurement of A_{PNC} possible, and it is the unique characteristics of the GaAs photoemission source that make it possible to meet the stringent requirements of this experiment.

Initially developed at Yale, the Bates source operates with a polarization of 0.36–0.40, provides preinjected peak currents up to 17 mA with pulse lengths of 15 μs and repetition rates up to 600 Hz. In a typical operating configuration the pre-injected peak currents are 9–11 mA. In addition, the source features a multichamber design that houses up to four GaAs crystals simultaneously. By virtue of this distinctive design, the lifetime of the source crystal can be studied in a more systematic fashion than would otherwise be possible.

2. Design considerations

With parity nonconservation measurements as the original motivation for its development, the Bates source was designed to meet the specific needs of the $\vec{e}$–^{12}C PNC experiment. Of course the source also had to meet the beam requirements imposed by the accelerator it serves, which in the case of the MIT Bates facility [25], a traveling wave linear electron accelerator, can be summarized as shown in table 1.

For a typical duty cycle of 1%, a maximum average current in the range of 50–100 μA requires that the current during the beam pulse must be in the range of 5–10 mA. With normal injection losses of ~ 66%, the polarized electron source must produce peak currents of 15–30 mA, with pulse lengths of 0–20 μs. In fact the parity experiment was designed with the assumption of a 20 mA peak current out of the source.

Since the parity experiment measures a very small helicity dependent cross section asymmetry, it is critical that the polarized electron source be free of helicity dependent variations in beam parameters such as intensity and direction. Beam loading effects, which make the accelerated energy E of the beam a function of the accelerated beam current I provide some insight into

Table 1
Accelerator and beam characteristics

Rf pulse length	0–30 μs
Pulse repetition rate, maximum	1 kHz
Transverse emittance	$10\pi/\gamma$ mm mrad
Energy spread for 80% current	0.2%
Injection energy	365 keV
Typical injection losses	66%
Beam duty cycle, typical	1%
Loading characteristic, $\delta E/\delta I$	~ 2.3 MeV/mA
Electron beam energy, unloaded, single pass, maximum	500 MeV
Electron beam energy, unloaded, recirculated, maximum	950 MeV
Electron beam energy, single pass, $I = 10$ mA, maximum	477 MeV
Average beam current, maximum ($I = 10$ mA, 1% duty)	100 μA

Table 2
Typical operating characteristics of polarized electron sources

Method of production	Average current	Peak current	Pulse length [μs]	Repetition rate [pps]	Method of helicity reversal	Phase space [$\pi m_e c$–cm]	Polarization
Field emission (EuS) [27,28]	10 nA	10 nA	cw	–	Magnetic	10^{-9}	0.85
Fano effect (Rb) [29,30]	18 nA	29 mA	0.012	50 pulsed laser	Optical	2.3×10^{-4}	0.65
Fano effect (Cs) [31]	25 nA	25 nA	cw	– arc lamp	Optical	$<4\times10^{-4}$	0.63
Optically pumped He discharge [32]	0.1 μA 50 μA	0.1 μA 50 μA	cw	– laser	Optical	2.5×10^{-5}	0.85 0.3
Polarized Li beam [33]	72 nA pre-injected	0.26 mA	1.6	180 flash lamp	Magnetic	$<1.710^{-3}$	0.85
Photoemission from GaAs (SLAC) [4,6,10]	7.7 μA injected	43 mA	1.6	180 pulsed laser	Optical	$<1.2\times10^{-3}$	0.4
Photoemission from GaAsP (Mainz) [34,35]	7 μA injected	35 mA	2	100 pulsed laser	Optical	not available	0.4
Photoemission from GaAs (Chalk River) [36,37]	350–700 μA pre-injected	350–700 μA	cw	– cw laser	Optical	not available	~ 0.35
Photoemission from GaAs (Bates)	110 μA pre-injected	11 mA (17 mA max.)	17 μs	600 modulated cw laser	Optical	$<1\times10^{-3}$	~ 0.35

the nature of the problem. At Bates, the beam loading is given by

$$\delta E/\delta I = -2.3\ \text{MeV/mA}, \tag{3}$$

and since the elastic scattering cross section for ^{12}C at 250 MeV exhibits an energy dependence given by an asymmetry

$$A = \frac{\delta\sigma}{2\sigma} = -2.5\frac{\delta E}{E}, \tag{4}$$

the variation in cross section $\delta\sigma$ depends on current fluctuations δI according to the relation

$$A = \frac{\delta\sigma}{2\sigma} = -5.8\frac{\delta I}{E}\ \frac{\text{MeV}}{\text{mA}}. \tag{5}$$

If A is to be maintained at the 10^{-7} level, eq. (5) immediately leads to the requirement $\delta I \leq 4.3\times10^{-6}$ mA for $E = 250$ MeV. In other words, for a peak accelerated current of 6.6 mA a fractional current fluctuation $\delta I/I = 6.5\times10^{-7}$ masks the parity asymmetry at a level of 10^{-7}. The requirement that helicity dependent current fluctuations be stable at this level places severe constraints on the method of helicity reversal.

An excellent summary of various techniques that have been used for producing polarized electrons had been given by Kessler [26]. In table 2 we summarize some of the characteristics of a number of different sources. Of the various approaches that have been tried, only the sources based on photoemission from GaAs have achieved the combination of the high peak currents and high average currents that are required at the Bates linac. GaAs sources also have the important advantage that they achieve the reversal of the electron helicity through optical means. Finally, it is possible to build GaAs sources such that their transverse phase space, or emittance, is quite small. Perhaps the largest drawback of GaAs sources is that, at present, their polarization is typically in the range of 0.3–0.45.

The intensity of a GaAs source is determined by the intensity of the radiation causing photoemission and the quantum efficiency of the photocathode. The quantum efficiency, QE, of a photocathode is defined as the number of electrons that are photoemitted divided by the number of photons that are incident on the crystal. In several of the GaAs based polarized electron sources that have been used at accelerators with short pulse lengths [4,6,10,34,35] pulsed lasers have been employed as the light sources. With such lasers, the high powers available makes it relatively easy to achieve high peak currents, and in some cases the sources are run at their perveance, or space charge, limit. The Bates requirement, however, is a pulse length of 15–20 μs with a repetition rate of at least 600 Hz. At the time the source was constructed there were no commercial pulsed lasers that met these requirements, thus making necessary the use of a cw laser, modulated to achieve the desired time

structure. We note that pulsed diode laser arrays may be a viable alternative in the near future. Although low in peak power the cw laser has the advantage of greater stability ($\sim 1\%$) during the beam pulse, thus permitting a small longitudinal phase space (energy spread) in the beam to be maintained.

The best source of cw radiation in the required wavelength range is a krypton ion laser. These lasers have two strong lines in the near infrared. The strongest line is at 752.5 nm, and the next strongest is at 799.3 nm. The two lines combined yield a power in the range of 1.5–3.0 W. A convenient expression for the photocurrent, I_{photo}, in terms of QE is

$$I_{\text{photo}}(\text{mA}) = P(\text{W})\lambda(\text{nm})\text{QE}(\%)8.065 \times 10^{-3}, \quad (6)$$

where P is the incident light intensity and λ is the wavelength of the light. Taking $\lambda = 752.5$ nm, $P = 1.5$ W, and assuming QE = 3%, which is reasonable, eq. (6) yields $I_{\text{photo}} = 27.3$ mA which exceeds the design goal mentioned earlier of 20 mA. This argument ignores the peak current limitations due to the perveance of the gun. Clearly, however, it is important to maintain both high laser power and high quantum efficiency. In fact, the combination of high peak current and high quantum efficiency achieved at Bates represents a new accomplishment in the field of GaAs polarized electron sources.

The high quantum efficiency of a GaAs photocathode results from a procedure that involves depositing cesium and an oxidizing agent on a clean GaAs surface. The quantum efficiency depends critically on a complex surface chemistry, and tends to decay with time. The required vacuum are on the order of 10^{-10} Torr, and the exact composition of the residual gases is very important. The characteristic time associated with the decay may be as short as minutes or as long as thousands of hours. It is often found that a short lived vacuum excursion can greatly decrease or even destroy the performance of a photocathode. For the Bates source where an excess in laser power does not exist, maintenance of an environment conducive to stable quantum efficiency takes on added significance. The photocathode must reside in a carefully controlled ultrahigh vacuum environment, and great care must be taken to have good differential pumping between the polarized electron gun and the inferior vacuum of the accelerator.

Given the fact that a photocathode's quantum efficiency will decay with a time that is short compared with most physics experiments, it is desirable to explore ways to decrease the "down time" associated with preparing new photocathodes. Several approaches may be taken. Two separate sources can be used, making it possible to switch back and forth as one becomes unusable. Alternatively, a single source can be designed with the capability of preparation and storage of more than one crystal at a time. In the former approach, one is faced with the cost of constructing two separate sources. In the latter approach, the single source will have a more complex design. With the high injection voltage at Bates, the latter approach appeared to be the most economical.

Handling and storage of more than one crystal is facilitated by the use of more than one vacuum chamber. In this way, one crystal can be prepared while another one is already in place and ready for use. If there were only one chamber, the preparation of the second crystal would adversely effect the first one. A multicrystal system also allows the ready comparison of different crystals, with regards to their performance characteristics. With the use of an airlock, GaAs samples may be loaded into the preparation chamber without ever breaking vacuum. There are advantages to a multichamber system in addition to the primary objective of handling more than one crystal. If the gun chamber, where the electron beam is produced, is coupled directly to a high gradient accelerator tube, as well as the rest of the beam line, the preparation of crystals in a separate chamber minimizes the frequency with which the gun chamber must be opened to air, and consequently the frequency with which it must be baked.

3. The principles of a GaAs polarized electron source

Photoemission from GaAs crystals has been described as a three-step process [38–40]: an electron absorbs a photon and is excited from the valence band to the conduction band, the electron diffuses to the crystal surface, and, finally, the electron escapes to the vacuum. The reason that the photoemitted electrons can be polarized is related to the initial excitation to the conduction band. The high quantum efficiencies result from achieving a negative electron affinity at the surface of the GaAs crystal.

GaAs is a direct band gap crystal. This means that the valence band maximum and the conduction band minimum both occur at the Γ point in the Brillouin zone, which is where the momentum vector of the electron $\boldsymbol{k} = 0$. The energy bands of a semiconductor do not in general have well defined angular momenta. At the Γ point, however, these symmetries are preserved, and well defined selection rules exist for the transitions. The energy band structure of GaAs in the vicinity of the Γ point is illustrated in fig. 1. At the Γ point the valence band has a P-like character, and the conduction band has an S-like character. The valence band is split by the spin–orbit interaction into a $P_{3/2}$ band, which is fourfold degenerate, and a $P_{1/2}$ band, which is twofold degenerate. The magnetic substates of the valence and conduction bands are shown at the right in fig. 1. If electrons are excited from the valence band to the conduction band using circularly polarized light of posi-

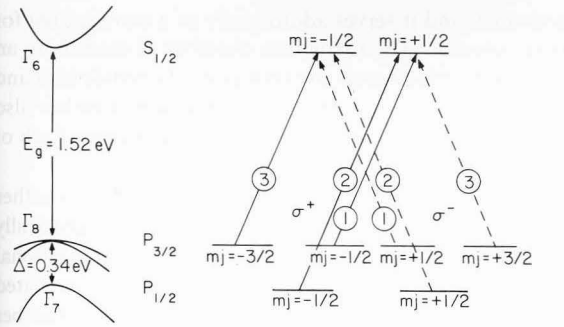

Fig. 1. At left are shown the energy bands of GaAs near the center of the Brillouin zone, the Γ point. The spin orbit splitting of the P valence bands and the degeneracy of the $P_{3/2}$ light-hole and heavy-hole bands are shown. At right, the magnetic sublevels are shown, labeled with the m_j quantum numbers. The relative transition probabilities are also shown for transitions between either the $P_{3/2}$ or the $P_{1/2}$ valence bands and the $S_{1/2}$ conduction band. Transitions allowed with σ_+ (σ_-) circularly polarized light are shown with solid (dashed) lines.

tive (negative) helicity, the selection rule $\Delta m_j = +1$ (-1) applies. The transitions obeying this selecting rule are shown with solid (dashed) lines. The strengths of these transitions are also indicated in fig. 1. When only transitions from the $P_{3/2}$ level to the $S_{1/2}$ are excited, the use of positive helicity light results in three times as many electrons arriving in the $m_j = -1/2$ state as in the $m_j = +1/2$ state. The polarization of an ensemble of electrons is defined by the equation

$$P = \frac{N_+ - N_-}{N_+ + N_-}, \tag{7}$$

where N_+ (N_-) is the number of electrons whose spins are aligned parallel (antiparallel) to the quantization axis. Using eq. (7) we see that the polarization of the electrons arriving in the conduction band is given by $P = (1-3)/(1+3) = -0.5$ for positive helicity photons. Similarly, negative helicity photons result in a conduction band polarization of $+0.5$. The relative strengths of transitions originating in the $P_{1/2}$ level are also shown in fig. 1; if electrons are also excited from this level, no polarization will result in the conduction band.

The high quantum efficiencies that are obtainable with GaAs result from creating a negative electron affinity (NEA) at the surface of a heavily p-doped crystal [38–40]. The key reason that an NEA surface results in high quantum efficiency is that a thermal electron then has sufficient energy to escape to the vacuum. The diffusion length of a thermal electron in the conduction band is roughly the same as the penetration depth of incident photons, about 1 μm. This means that a large fraction of the electrons that are excited to the conduction band are able to diffuse to the surface and escape.

The NEA is obtained through a process often called activation. The process consists of depositing layers of cesium and either oxygen or fluorine onto the crystal surface. The deposition can proceed only when the surface is clean. Clean GaAs has an electron affinity of about 4 eV. (The electron affinity is the energy difference between the conduction band and the vacuum.) When cesium alone is deposited on the surface, the electron affinity is lowered to within a few tenths of an eV of zero. When both cesium and oxygen (or fluorine) are deposited on the surface, the electron affinity actually becomes negative.

There are several depolarization mechanisms that reduce the emitted electrons polarization below the theoretical maximum of 50%. The dominant effect is related to the excitation process. If the absorbed photon has an energy that is larger than the band gap energy, the excitation to the conduction band does not occur exactly at Γ. Away from Γ, the $P_{3/2}$ band is mixed somewhat with the $P_{1/2}$ band, and as was discussed above, this permits additional transitions to the undesired magnetic sublevels, resulting in a reduction of the polarization. As the photon energy increases still further, the transitions occur at Γ, but from both the $P_{1/2}$ and the $P_{3/2}$ bands, and the polarization goes to zero. Photons that are just above the band gap energy result in the highest polarization. The quantum efficiency however, increases sharply as the photon energy is increased above E_g. A "trade-off" must be reached: the photon energy must be high enough to produce high yield, and yet low enough to produce good polarization. Other depolarization effects can also occur while the electrons are diffusing through the crystal bulk toward the surface. The mechanisms responsible are temperature dependent, and can be suppressed by operating the source in the vicinity of liquid nitrogen temperatures, resulting in a 20% improvement in the polarization [5]. The effect of the depolarizing mechanisms that occur while the electrons are diffusing can also be minimized by ensuring that the electrons cannot diffuse very far. This can be accomplished by the use of epitaxially grown GaAs in which a *blocking layer* of GaAlAs just below the surface of the crystal prevents electrons from deep within the bulk of the crystal from diffusing to the surface. The resulting crystal will have a lower quantum efficiency, but will yield high polarizations [41]. It has also been suggested that the polarization is material dependent [42]. If the spin relaxation time is long compared to the conduction band lifetime, better polarization results. Unfortunately, this also means that crystal with particularly high yield, and hence long conduction band lifetimes, may exhibit lower polarization.

4. The Bates GaAs polarized electron source

4.1. The layout of the source

The source is mounted on a high voltage platform that is surrounded by a Faraday cage maintained at approximately -300 kV relative to ground. As shown in fig. 2, the platform is supported by four large insulating legs that are surrounded by two sets of corona rings, one outside the supporting legs and one inside the supporting legs. The high voltage is produced by an insulating core transformer, and the ac power for the equipment within the Faraday cage is supplied by a separate isolation transformer.

The vacuum system of the source includes three separate chambers – the gun chamber, the preparation chamber, and the extraction chamber. The gun chamber, as the name suggests, is where the electron beam is actually produced when the source is in operation. It houses the electrodes which are used to extract the electrons from the crystal and form them into a beam. The preparation chamber is where the crystals are activated, and it serves additionally as a storage area for spare crystals. The extraction chamber is essentially an air lock that facilitates the transport of crystals into and out of the vacuum system. The extraction chamber also plays an essential role as a gas handling system. Each of the three chambers is indicated in fig. 2.

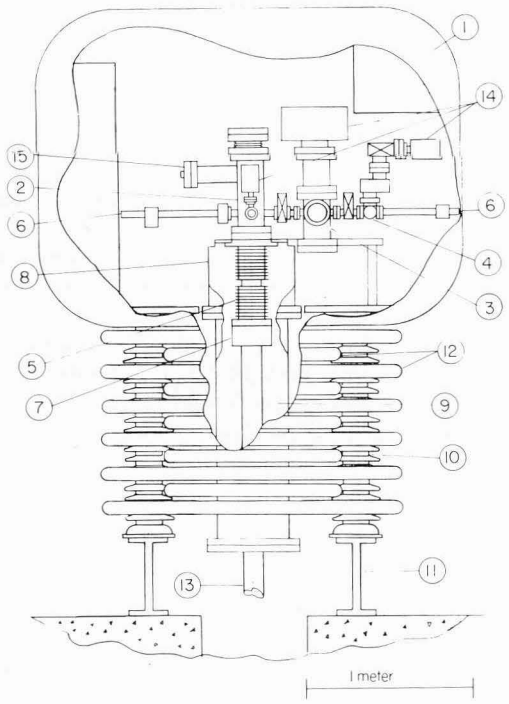

Fig. 2. The layout of the source showing the Faraday cage (1), the gun chamber (2), the preparation chamber (3), the extractor region (4), the accelerator column (5), two magnetically coupled manipulators (6), solenoid #1 (7), the SF_6 pressure vessel (8), the interior of the pressure vessel containing SF_6 (9), the insulating legs (10), the I-beams (11), the corona rings (12), the beam line to the accelerator (13), ion pumps (14), and the extention of the gun chamber that contains the titanium sublimation pump (15).

The crystals are moved from one chamber to another using a transport system containing two magnetically coupled manipulators that provide both translational and rotational motion. The manipulators are indicated in fig. 2. The preparation chamber and the gun chamber are both equipped to receive crystals from the manipulators and move them about as necessary. The crystal transport system is the subject of section 4.4.

Immediately below the gun chamber is a 300 kV accelerator column. As can be seen from fig. 2, the bottom of the accelerator column, which is at ground potential, is physically quite close to the bottom of the Faraday cage. In order to prevent arcing, the accelerator column is surrounded by 5 atm of SF_6. The gas is contained in a pressure vessel, the top portion of which is aluminum and is maintained at the same potential as the source. The bottom portion of the pressure vessel, which must be an insulator (since one end is connected to the source and the other end is connected to ground), is made of fiberglass.

4.2. The preparation chamber

The preparation chamber contains all the necessary hardware for activating crystals. It also functions as a staging area, providing the flexibility for in vacuo storage of more than one crystal at a time. A crystal may be prepared in the preparation chamber while a second previously prepared crystal is stored in the gun chamber. Crystals must be prepared one at a time because the activation process adversely affects other previously prepared crystals.

The crystals are mounted in crystal holders, three of which are visible in fig. 3. The holders, fabricated from molybdenum and surrounded by an OFHC copper bushing, are stored on a rotatable carousel, which allows them to be positioned in any of four locations. The crystal at the left in fig. 3 is in position for activation; the crystal on the right is shown in the process of being transported to another chamber. Each crystal, 15 mm in diameter and 0.64 mm thick, is supported by a lip at the open bottom of the holder and is held firmly in place by a stainless steel clamping disk from above. A molybdenum washer is usually inserted between the crystal and the lower supporting lip of the crystal holder to limit the emitting area of the crystal. The carousel can hold one crystal holder on each of four arms, three of which are visible in fig. 4. The carousel is coupled to a rotational motion feedthrough. At each of the locations where crystal holders are stored, there is a small

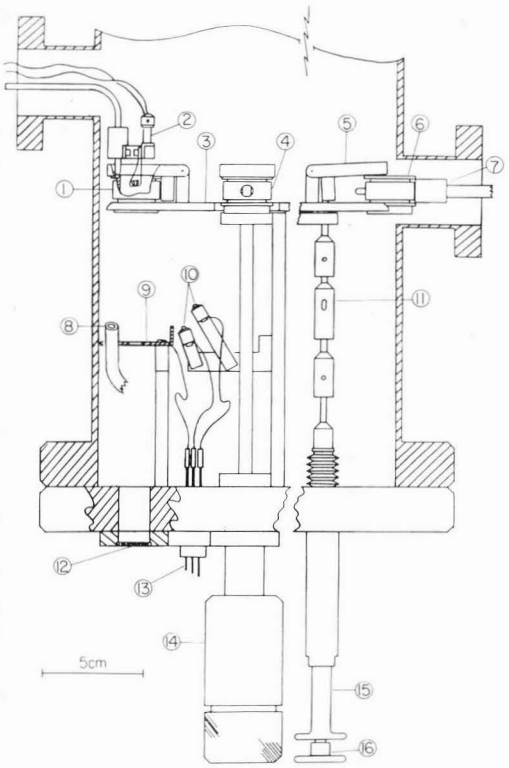

Fig. 3. The preparation chamber showing a crystal in position for activation (1), the moveable thermocouple and filament assembly (2), the carousel (3), another crystal holder (4), a cage in the up position (5), a crystal holder in the process of being transported (6), one of the spears attached to a manipulator shaft (7), the gas line for NF_3 or O_2 (8), the Faraday cup (9), the Cs dispensers (10), a spring loaded coupler for the pusher that is used for lifting the cages (11), a view port (12), an electrical feedthrough (13), rotational motion feedthrough (14), the moveable pusher (15), the pusher release (16).

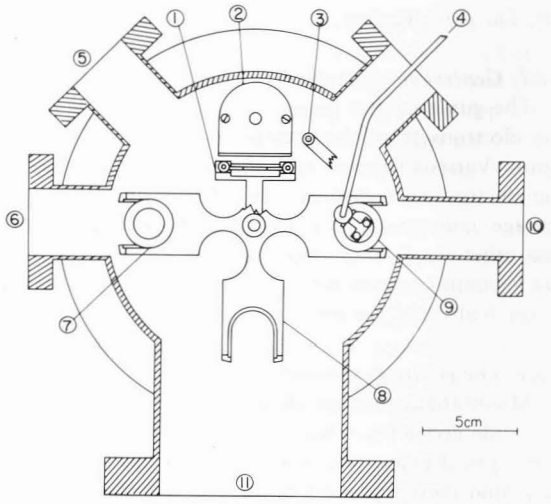

Fig. 4. Top view of the preparation chamber showing one of the two Cs dispensers (1), the Faraday cup (2), the NF_3/O_2 gas line (3), one of the two moveable thermocouple/filament assemblies (4), the port on which the other thermocouple/filament assembly is mounted (5), the port leading to the gun chamber (6), a crystal holder (7), the carousel with one of its four arms cut away to show components below (8), a crystal holder in position to be flashed (9), the port leading to the extractor airlock (10), and the port used for the viewport (11).

cage that fits loosely over the top of the crystal holder to prevent it from slipping out of position. In fig. 3, on the right, a cage is shown in the up position. The other cages in the figure are in the down position. The cages are actuated by small pushers operated from outside the vacuum system.

A flash assembly is used to heat-clean each crystal prior to activation. Heat cleaning involves raising the temperature of the crystal to between 550–610 °C, at which point oxide layers that are on the surface of the crystal vaporize. The crystal is brought up to temperature by the radiant heat of a filament which is lowered into the top of the crystal holder. The crystal holder and crystal eventually achieve thermal equilibrium; then the temperature of the crystal can be monitored by a thermocouple probe in contact with the upper lip of the crystal holder. When the carousel is rotated, the thermocouple/filament assembly must be lifted out of the way. The mechanical support for the thermocouple/filament assembly is entirely external to the vacuum system, incorporating a bellows that allows the assembly to be moved under vacuum. There are two flash assemblies mounted on the preparation chamber, one of which is shown in the top view of fig. 4. A side view is shown in fig. 3.

The bottom flange of the preparation chamber has three "Mini Conflat" ports that accommodate the components needed for the activation of the crystal, including a four pin electrical feedthrough that is connected to two Cs dispensers * and a Faraday "cup", a window that admits light to the crystal, and a gas line that directs O_2 ** or NF_3 onto the crystal. The flange also contains two additional ports, one simply acting as a spare and the other providing electrical contacts to a third Cs dispenser used for initial "seeding" of the chamber. The distance between the crystal and either the gas line or the Cs dispensers used for activation is between 4 and 6 cm. The Faraday "cup" is actually a ring through which light can pass onto the crystal, as shown in fig. 4.

* The cesium dispensers are furnished by SAES/USA Inc., of Colorado Springs, Colorado, USA, model #641204.

** The oxygen is research grade, 99.99% pure. The NF_3 is MOS grade.

4.3. The gun chamber

4.3.1. General considerations

The gun chamber houses the electrodes that extract the electrons from the crystal and focus them into a beam. Various support and alignment mechanisms for the electrodes are included. In addition, there are high voltage connectors, devices for transporting crystals, and other small components needed for operation. All the vacuum components are compatible with pressures in the high 10^{-11} to low 10^{-10} Torr range.

4.3.2. The electrode geometry

Much about the gun chamber is determined by the electrode geometry, which must have well defined electron optical properties. The electrodes must be shaped such that they produce a beam with a transverse phase space that matches the acceptance of the accelerator. The electrodes must also have a high perveance; that is, they must be capable of producing adequate peak current with reasonable extraction voltages. The design of the original Bates thermionic gun utilized a Pierce-style geometry to achieve these results [43,44]. The Pierce geometry has the advantage that the electric fields are shaped to compensate, at least in part, for space charge effects produced by the mutual repulsion of electrons [45,46]. Since the existing thermionic gun has satisfactory, well understood properties, we used it as a starting point for the design of the electrode geometry for the polarized electron gun.

Although one would want the polarized electron gun to be as similar as possible to the thermionic electron gun, there are several differences in the design, some of which are related to ultrahigh vacuum requirements. The accelerator column of the thermionic source, for example, could not be duplicated because epoxy was used in its construction. Thus a column of somewhat greater length and somewhat lower gradient had to be used. It was also necessary that a 1 cm aperture be included at the top of this column for differential pumping purposes. In addition, the surface requirements of a GaAs photocathode dictated the use of a more open anode geometry in order to minimize the possibility of beam scraping.

Another significant difference is that a thermionic cathode generally has a fairly uniform current distribution across the emitting surface, whereas a photocathode has, in general, a nonuniform distribution. The nonuniformity arises from the fact that the local emission current density is roughly proportional to the power density of light, at least until saturation is reached. Since the laser spot is roughly Gaussian, below saturation, the current density will be roughly Gaussian.

Saturation, or space charge limitation occurs when the electron density just outside the cathode surface cancels the electric fields due to the electrodes. The saturation current is given as a function of voltage by the relationship [46,47]

$$I_{SAT} = KV^{3/2}, \tag{8}$$

where the constant K is called the perveance and is a property of the electrode geometry. The maximum current density at any point on the cathode will be approximately I_{SAT}/A, where A is the area of the cathode. Thus, under conditions of saturation the current distribution from a photocathode will be a Gaussian with a flattened top at I_{SAT}/A.

The differences between the thermionic gun and the polarized gun necessitated a design study, which was undertaken with the use of the SLAC Electron Trajectory Program [48]. The first design efforts focused on electrodes that were liquid nitrogen cooled, since the polarization of GaAs sources has been reported to be about 20% higher when operated at liquid nitrogen temperatures [5]. Although the design was ultimately abandoned for reasons of vacuum integrity, the results, summarized elsewhere [49,50], demonstrated the importance of accelerating the beam in a relatively short distance. As the acceleration distance was lengthened, the phase space of the beam increased due to space charge effects.

The critical nature of space charge effects became even more apparent during later studies which led to the room temperature design currently employed [51]. These studies for the first time examined the effect of the nonuniform Gaussian current distributions obtained with laser photoemission and revealed a strong dependence of the phase space on the size of the laser spot. A geometry was developed that had acceptable properties when the crystal was illuminated with a laser spot characterized by a $1/e^2$ intensity radius of 3.73 mm. This spot size results in 90% of the laser beam falling within the 4 mm radius of the cathode. A composite of several ray trace runs is shown in fig. 5.

In the early stages of operation of the source, it was observed that the 1/e-lifetime of the quantum efficiencies of the crystals never exceeded 4–5 h. Additional ray trace studies were undertaken to test the hypothesis that the detailed structure of the cathode in the immediate vicinity of the crystal might be producing a very low current halo that, after impacting with nearby metal surfaces, would cause the desorption of damaging residual gases. The studies supported the existence of a halo, and crystal holders were modified to include molybdenum washers to limit the emission area to about 5 mm. This technique proved successful in greatly increasing lifetimes to those reported in section 6.

4.3.3. The electrode assembly

The electrode assembly is suspended from a single 8 in. Conflat flange at the top of the chamber. The 8 in. flange includes the necessary high voltage and mechani-

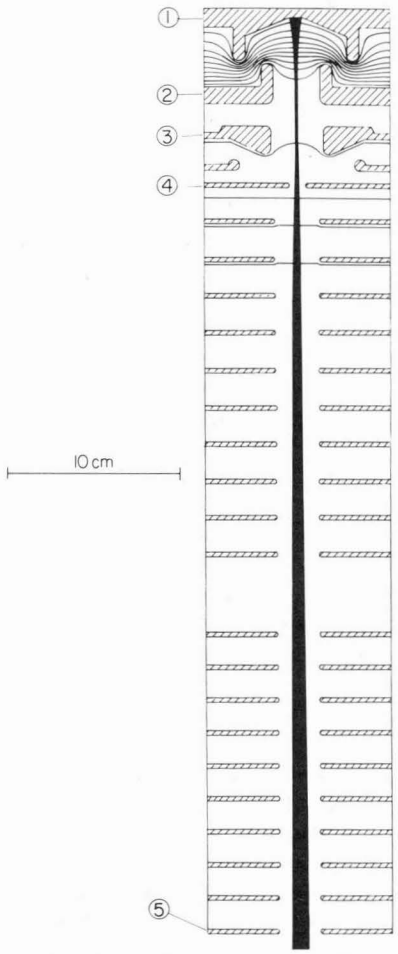

Fig. 5. Composite of several ray traces of the Bates polarized electron gun. Shown are the cathode (1), the anode at 10 kV (2), the third electrode at 15 kV (3), the beginning of the accelerator column at 25 kV (4), and the end of the accelerator column at 365 kV (5). The beam is 20 mA, and has a Gaussian current distribution. We note that in practice we run with somewhat lower voltages.

cal feedthroughs, making the electrode assembly a self contained unit that can be installed or removed with relative ease.

There are three electrodes – the cathode, the anode, and a "third electrodes". The electrodes are stacked in sequence inside an insulating Macor cup, separated from each other by macor spacers. The Macor cup is suspended by a ladder structure from the top flange. In fig. 6 the Macor cup and the various component parts of the ladder structure are clearly indicated. The lower ladder plate, connected to the cathode by stainless steel rods, is maintained at a voltage of -18 kV with respect to the gun chamber wall during operation. The upper ladder plate, connected to the top flange by stainless steel rods, is connected to the lower ladder plate by insulating posts made of Steatite.

A detailed view of the electrode region is shown in fig. 7. Note that the electrode stack is supported from below by a lip on the Macor housing, and is held fixed by a stainless steel split retaining ring at the top. (The tolerances were chosen to account for thermal expansion that takes place during bakeouts.) The high voltage connection to each of the electrodes is made by an MDC model #HVC-150 feedthrough, mounted on the top flange, in conjunction with a 1/16 in. diameter stainless steel rod, insulated with alumina tubing, that connects the electrode to the feedthrough.

Since the lower ladder plate is at the same potential as the cathode, the higher voltage contact to the cathode is actually made at the lower ladder plate. The other

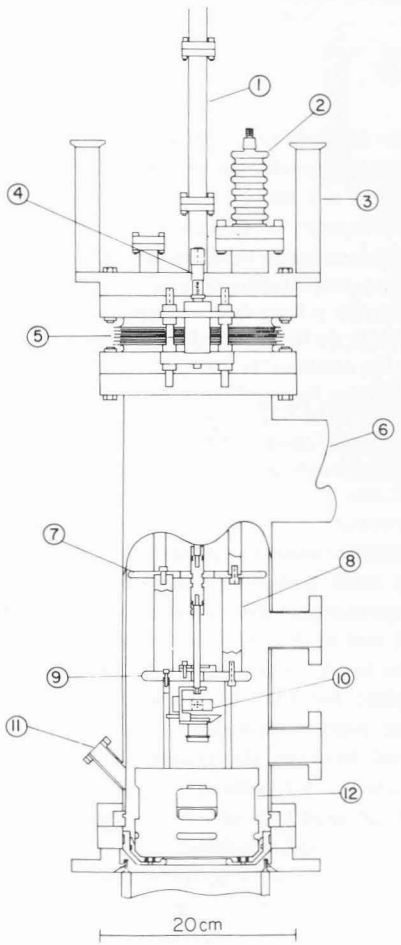

Fig. 6. The gun chamber, emphasizing the mechanical aspects of the electrode assembly. Shown is the spool piece for the plunger's linear motion feedthrough (1), a high voltage feedthrough (2), a handle for supporting the electrode assembly during installation (3), a micrometer (4), the bellows assembly (5), an extension that houses a titanium sublimation pump (6), the upper ladder plate (7), the steatite insulators (8), the lower ladder plate (9), the plunger (10), a peep port (11), the Macor housing for the electrodes (12).

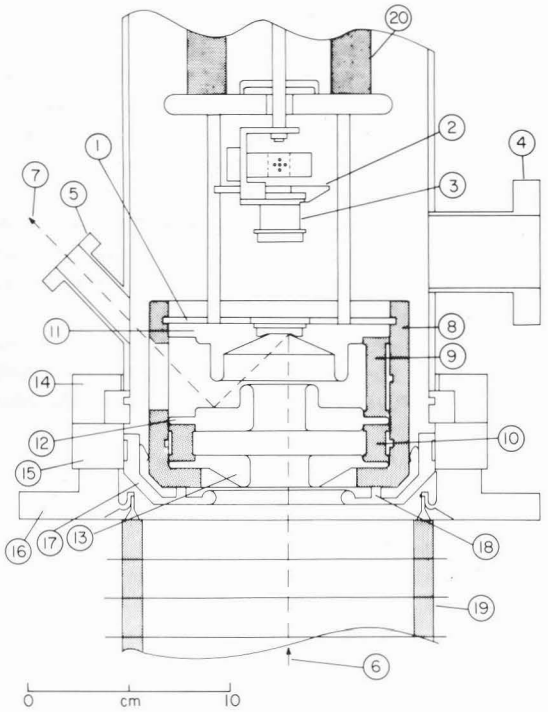

Fig. 7. Electrode region detail showing the split ring (1), the plunger (2), a crystal holder (3), a port for crystal transport (4), a peep port (5), a laser beam extreme ray (6), a laser beam pickoff ray (7), the Macor cup (8), a Macor spacer (9), a Macor ring (10), the cathode (11), the anode (12), the third electrode (13), the bottom flange of the gun chamber (14), the double sided flange (15), the top flange of the accelerator column (16), and the electrode support shelf (17), a guidance pin (18), the accelerator column (19), and a ceramic post (20).

two electrodes require connections that penetrate the electrode stack with each connecting rod anchored at two locations: each rod is screwed into its respective electrode and each passes through a snug Macor bushing in the lower ladder for the anode and in the upper ladder plate for the third electrode. Except for the anchoring points, clearance of several millimeters is maintained between the alumina tubes and all other metal surfaces. All metal surfaces at which there are high voltage gradients are machined to a "63" finish and electropolished, resulting in mirrorlike finishes.

The maintenance of gradients in our system was made more complicated by the introduction of Cs into the system. Cs lowers the work function of metalic surfaces and provides conducting paths on insulating surfaces, thus making breakdown and glide discharge more likely to occur. A great deal of care was taken to avoid the existence of likely breakdown paths. In fig. 7, for instance, it can be seen that all the Macor spacers have grooves machined into them so that there is never a straight path along a ceramic between two metal surfaces at different potentials. Similarly, the Steatite posts that connect the upper and lower ladder plates are mounted in machined seats, so that at the point where the ceramic touches the metal, there is nearly zero electric field that could initiate a glide discharge.

The electrodes must be properly aligned when they are installed. Guidance pins attached to a double sided flange at the bottom of the chamber are used for this purpose as shown in fig. 7. There are four pins on the double sided flange, only two of them provide guidance, with all four of them providing support. The four pins are precision custommade shoulder bolts. Captured beneath each head is a precisely machined flat washer, and beneath each flat washer is a stack of six Belville washers. The result is that the four flat washers form a spring loaded platform that is precisely positioned under compression. Great care must be taken during assembly, however, that the electrode structure is not put under too much compression. There is an adjustable bellows assembly at the top of the gun chamber that can be used to locate the electrodes properly. Three jacking screws can be adjusted with the help of three micrometers to provide a reference. It is important to make the necessary adjustments while the system is at air pressure, so that no undue stresses occur after the system is pumped out.

4.3.4. The gun chamber cesiator

Cs can be introduced into the gun chamber by dispensers identical to those used in the preparation chamber. The dispensers are mounted on an eight pin feedthrough, connected to a linear translator. When the dispensers are moved into the chamber, the cesium is emitted in the general direction of the gun chamber wall, just above the level of the electrode stack. Care is taken not to deposit Cs in areas with large voltage gradients. The Cs is used to extend crystal lifetimes in the gun chamber [52].

4.4. The crystal transport system

Crystals are moved between chambers by means of two magnetically coupled manipulators, one of which is attached to the gun chamber, and the other of which is attached to the extraction airlock. Both are visible in fig. 2. Attached to the end of each manipulator is a spear mechanism, shown in fig. 8, that mates with the crystal holders. The spears can be rotated into a lock or unlock position.

There must be a receiving point in each chamber where transported crystals are deposited. In the preparation chamber the carousel serves this function. In the gun chamber there is an assembly called the plunger which is used to lower the crystal into the electrodes. In fig. 7, a crystal holder is shown in the plunger, ready to be inserted. Fig. 8 shows the plunger in detail, and illustrates its interaction with the spear and the crystal

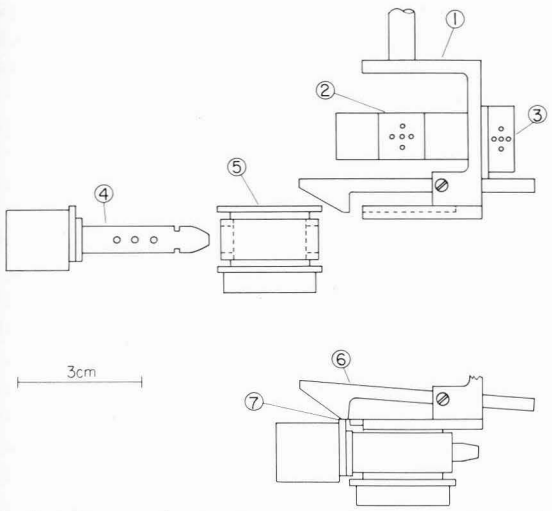

Fig. 8. A diagram showing the plunger (1), and attached to the plunger, the primary laser target (2), and the crystal transport laser alignment target (3). Also shown is the gun spear (4), and a crystal holder (5). At the bottom of the diagram, the plunger's latch (6), is shown being lifted by the spear's cam (7).

holder. The bottom of the plunger is shaped like a horse shoe, and supports the crystal holder from a top lip. The plunger has a gravity actuated latch for securing the crystal holder. An eccentrically shaped cam on the spear provides a means for lifting the latch when the crystal holder is removed. At the bottom of fig. 8, the crystal holder is shown in the plunger, about to be removed, with the cam lifting the latch.

Another important feature of the plunger is the primary laser target. When there is no crystal holder in the plunger, this target is exposed through the horse shoe shaped bottom of the plunger. The laser that normally hits the crystal can thus hit the target. The target provides the primary means for centering the laser on the crystal.

In order for crystals to be transported smoothly, the vacuum chambers of the source and the magnetically coupled manipulators must all be carefully aligned. This is accomplished by using a small HeNe laser and a system of collimators and laser targets. The collimators are attached to the flanges of the vacuum system, and the chambers are adjusted in position until the laser can be threaded through them. Once this is accomplished, the laser beam is deflected into the vacuum system using two pentaprisms, and is used for sighting the position of the manipulators with respect to the plunger and the carousel. The spear attached to the gun manipulator, the plunger, and the carousel all incorporate small targets for sighting the position of the laser beam.

4.5. The optics system

4.5.1. Layout

The optics system contains a cw krypton ion laser; an electro-optical shutter; two helicity reversing devices, one fast and one slow; a lens system for focusing the laser beam onto the crystal; and an optical transport system that carries the laser beam from an optics table to the crystal along a 14.5 m path. The layout of the optics table is shown in fig. 9.

4.5.2. The laser

The laser, a Coherent model #CR-3000K, is a cw krypton ion laser with a graphite plasma tube. It has two useful lines, one at 752. 5 nm, and once at 799.3 nm. (A third line at 793.1 nm has a much reduced intensity.) The laser may be operated in either a single line mode, or a multiline mode. In the multiline mode, the two lines in the near infrared produce between about 1.5 and 3.0 W. Typically, in single line operation,

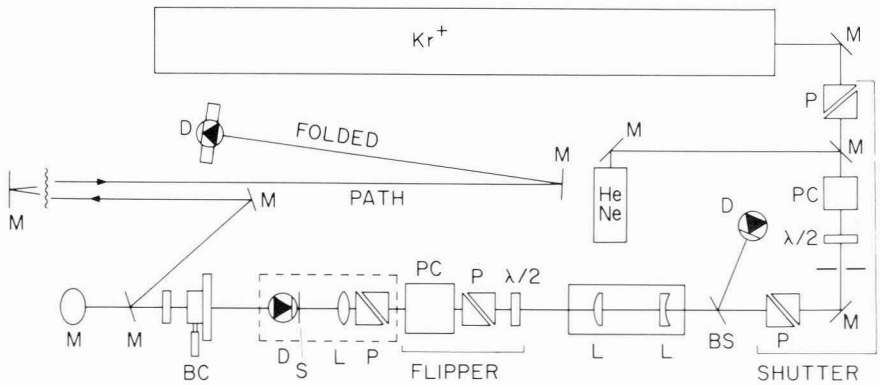

Fig. 9. Laser table layout showing mirrors (M), polarizers (P), Pockels cells (PC), lenses (L), half-wave plates (λ/2), a beam splitter (BS), and photodiodes (D). Also shown is a krypton ion laser and a HeNe alignment laser. The optical elements labeled *flipper* are used for reversing the helicity of the light. The optical components labeled *shutter* comprise an electro-optical shutter that is used to modulate the cw krypton ion laser light into pulses.

the 752 line produces about 1.4–1.6 W, and the 799 line produces 0.4–0.5 W.

The properties of the laser cavity, which are important for focusing calculations, are determined by the cavity mirrors and the cavity length. When the near infrared lines are being used, the front mirror, the output coupler *, has a 10 m radius of curvature, and a transmittance for the near-infrared lines of 1.3%. The rear mirror ** has a 10 m radius of curvature, and a transmittance $< 0.3\%$. The length of the cavity is about 1.8 m. In this configuration the waist will occur at the center point of the cavity, and for the 752 nm line, the radius of the waist, w_0, can be calculated to be 0.83 mm using the formula [53,54]

$$w_0 = \left(\frac{2\lambda\sqrt{RZ - Z^2}}{2\pi} \right)^{1/2}, \tag{9}$$

valid for a symmetric laser cavity whose mirrors both have a radius of curvature R, and whose length is given by $2Z$.

The manufacturer specifies the laser noise to be less than 1% in a current regulated mode, and less than 0.5% in a light regulated mode. We found that the laser power oscillated at low power in the light regulation mode. In either mode, the noise appeared to be less than about 1% at full power; at low power the noise appeared to be higher.

4.5.3. The electro-optical shutter

The electro-optical shutter contains two crossed polarizers + separated by a double crystal Pockels cell. When the Pockels cell is off, the crossed polarizers block the beam. When the Pockels cell is pulsed at the appropriate voltage, it behaves as a half wave plate, and the polarization vector of the beam is rotated by 90°, thus allowing the beam to pass through the second polarizer with minimal losses. The fast and slow axes of the Pockels cell are oriented at $\pm 45°$ to the two axes defined by the polarizers. For minimal insertion loss from the shutter, the first polarizer is oriented to match the output of the laser, which is highly linearly polarized.

The Pockels cell ++ has an aperture 10 mm in diameter and contains windows which are made of fused silica, coated with a V-type antireflection coating centered for 700–800 nm. The device has a measured contrast ratio exceeding 600:1. The driver for the Pockels cell * is a high voltage pulse generator that uses a TTL input trigger, and produces a high voltage pulse of 0–4 kV. The pulse length can be varied between 8 and 23 μs. The rise time is less than 1 μs.

4.5.4. Helicity reversal

Fast helicity reversal is accomplished through the use of a second Pockels cell. Just as the Pockels cell in the shutter acts as a pulsed half wave retarder, the helicity reversal Pockels cell acts as a pulsed quarter wave retarder. The polarity of the voltage used to drive the Pockels cell determines the helicity of the resultant circularly polarized light. Through the use of a bipolar driving system that is triggered by TTL signals, the helicity of each beam pulse can be arbitrarily selected.

The Pockels cell that is used for producing the circularly polarized light is a Cleveland Crystals model #TX 2042. Having a specified contrast ratio of 3450:1 and very good uniformity of retardation across a 20 mm aperture, this Pockels cell has characteristics that play an important role in controlling systematic errors. The Pockels cell mount, moreover, provides angular adjustment about all three axes as well as translation along all three axes, thereby allowing the crystal to be scanned for a "best spot" with respect to eveness of retardation. Two different systems for supplying bipolar high voltage pulses to the Pockels cell have been used. One system employs two dc high voltage power supplies of opposite polarity, and a high voltage switch. The switch has two TTL inputs, one for each polarity. With this system, the stability of the voltage applied to the Pockels cell is determined by the stability of the power supplies. This is the system that has been used for parity violation measurements. The second system for supplying bipolar high voltage pulses utilizes a commercial high voltage amplifier **. The amplifier requires an input voltage of several volts and amplifies it to several kilovolts, with a gain of about 1500. The disadvantage of this approach is that any noise or drift at the input is amplified. The Møller measurements presented in section 6 were made using the high voltage amplifier.

It is important to have more than one means of reversing the helicity of the light. To this end the optics system contains a half wave plate upstream of the Pockels cell quarter wave retarder, as shown in fig. 9. The half wave plate provides a slow reversal of the helicity state as opposed to the rapid reversal that is possible with the Pockels cell. A linear polarizer is used after the half wave plate to ensure a high degree of linear polarization going into the Pockels cell.

* Coherent model #903-065.
** Coherent model #903-064.
+ Special Optics model #M7-1210-750, Glan-Laser Air Spaced Polarizers (also known as a Glan–Foucault or Glan–Air polarizer [55]).
++ Lasermetrics model #1042 FV.

* Lasermetrics model #8019.
** Lasermetrics Inc. model #8403M.

4.5.5. Systematic control and the PITA effect

It is extremely important that all characteristics of the laser beam illuminating the crystal, such as position and intensity, be stable against helicity reversal. Any systematic helicity correlated effects can generate false asymmetries that mimic parity violating asymmetries. One such source of systematic error is a helicity correlated intensity fluctuation, that can be caused by a polarization induced transport asymmetry (PITA). A more detailed analysis of the PITA effect appeared elsewhere [56], but a brief description of the effect will be given here.

The PITA effect arises because any optical transport system for linearly polarized light has an efficiency that is a function of the orientation of the polarization axis. Let us say that we choose a set of axes such that maximum transmission, $T_{x'}$, occurs for light polarized along the x' axis, and minimum transmission, $T_{y'}$, occurs for light polarized along the y' axis. We can characterize the transport asymmetry (for linearly polarized light) by the parameter ϵ defined by

$$\epsilon = \frac{T_{x'} - T_{y'}}{T_{x'} + T_{y'}}. \tag{10}$$

Perfectly circularly polarized light is insensitive to this transport asymmetry, but for any practical beam there will always be a small admixture of linear polarization, giving rise to elliptical polarization.

Consider the configuration illustrated in fig. 10a. The direction of the propagation of the light is along the z-axis, with the light initially polarized at 45° with respect to the x-axis. The light first passes through a Pockels cell, acting as a pulsed quarter wave retarder, whose fast axis is along the y-axis. Following the Pockels cell the light passes through a transport system, characterized by a transmission reference axis x' making an angle Θ with respect to the x-axis.

The positive and negative retardations δ_+ and δ_- introduced by the pulsed Pockels cell can be expressed in the general forms

$$\delta_+ = +\left(\frac{\pi}{2} + \alpha\right) - \Delta, \tag{11}$$

and

$$\delta_- = -\left(\frac{\pi}{2} + \alpha\right) - \Delta, \tag{12}$$

where α and Δ are two independent parameters. When $\alpha = \Delta = 0$, perfectly circularly polarized light is obtained, the appropriate ellipses for describing the polarizations reducing to two circles, as indicated in fig. 10b. When $\Delta \neq 0$, elliptically polarized light results, with the principal axis of the ellipses having a different tilt for each helicity state, as indicated in fig. 10c. Light that is associated with an ellipse whose principal axis is more closely aligned with the axis, x', of the transport system

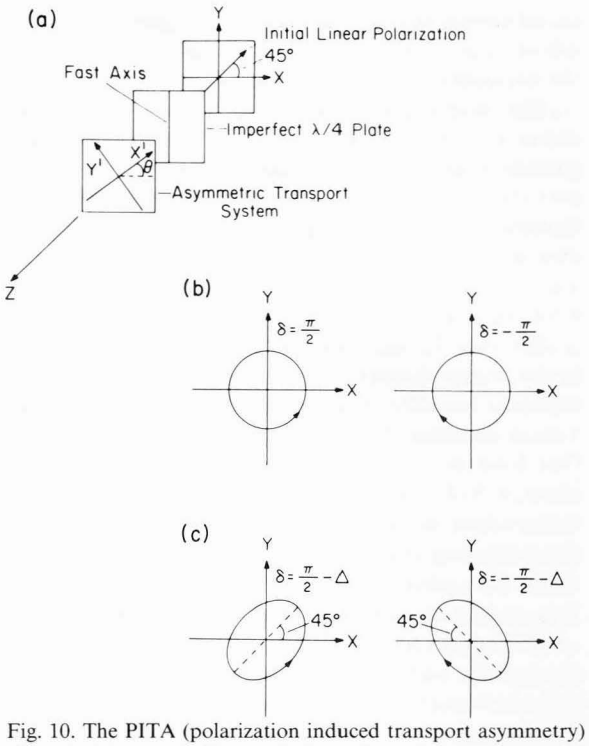

Fig. 10. The PITA (polarization induced transport asymmetry) effect is illustrated. The optical configuration is shown (a), along with the ellipses associated with perfectly circularly polarized light (b), and imperfectly circularly polarized light (c).

will clearly be transported more efficiently than light associated with an ellipse whose principal axis is more closely aligned with y'. The asymmetry in the intensity of light that is transmitted through the transport system under these conditions is then given by [56]

$$A_{\mathrm{PITA}} = \frac{I_+ - I_-}{I_+ + I_-} = \frac{\Delta\epsilon}{T}\sin(2\Theta), \tag{13}$$

where T is the average transmission of the x' and y' axes.

As discussed earlier, a helicity correlated intensity fluctuation produces an asymmetry in the data that mimics a parity violating asymmetry. There are at least three ways that A_{PITA} can be made small. First, a transport system can be developed to produce a small value of ϵ. Second, an optical arrangement can be used to minimize Δ by making it an adjustable parameter. Finally, a half wave plate can be used to rotate the axes of the ellipses such that their principal axes are aligned with the x and y axes instead of the x' and y' axes [34,35].

There are two ways in which Δ may be made an adjustable parameter. One way is to include a Babinet–Soleil compensator in the system (see section 6) as shown in fig. 9. The compensator can be adjusted

to introduce any Δ that is desired. Another way to adjust Δ is to rely on the Pockels cell itself and make the adjustment electro-optically.

The foregoing analysis of the PITA effect is by no means complete, since in general there will be several sources of phase shift associated with different transport elements, each with its own set of reference axes. However, many optical transport systems, including our own, are adequately described by this formalism.

4.5.6. The laser beam transport and focusing system

The laser beam is transported from the optics table to the crystal through a remotely adjustable laser beam transport line. The transport line contains four mirrors, 1 in. in diameter. Two kinds of mirrors have been tried. One kind is coated with silver and overcoated with about a 1/4 μm layer of thorium fluoride *. These mirrors have the advantage that their reflective properties, including induced phase shifts, can be computed easily. The other kind of mirrors have dielectric coatings, and are more efficient reflectors.

It is critical that the laser spot size on the crystal be controllable and well understood. The aperture in the cathode through which the crystal is exposed is 8 mm in diameter. When a molybdenum mask is employed, the clear aperture is 4–6 mm. Thus, among other things, the spot size determines the fraction of the laser spot that will actually illuminate the crystal. As mentioned in the section on the electrode geometry, the spot size is also an important factor in determining the electron optical properties of the beam. The spot size is controlled by two lenses on the optics table. By moving the two lenses with respect to each other, the spot size on the crystal can be made quite small, or arbitrarily large.

The focusing properties of the lenses can be studied with the use of a folded optical path. The folded path uses several mirrors to create a path length that is equivalent in distance to that required for transport to the crystal. The folded path is shown schematically in fig. 9. The folded path is used on one hand to preserve alignment when adjustments are made on the laser table, and on the other hand to scan the laser profile in a qualitative fashion.

4.6. The polarized injector beam line

The beam line that connects the polarized injector to the accelerator serves several important functions. It contains focusing and steering elements, as well as diagnostics for monitoring the beam, and with the use of differential pumping, helps isolate the ultrahigh vacuum of the source from the poorer vacuum of the accelerator. It also contains the provision for a Wien Filter [57], which, in the future, will be used to rotate the spins of the electrons by means of crossed electric and magnetic fields.

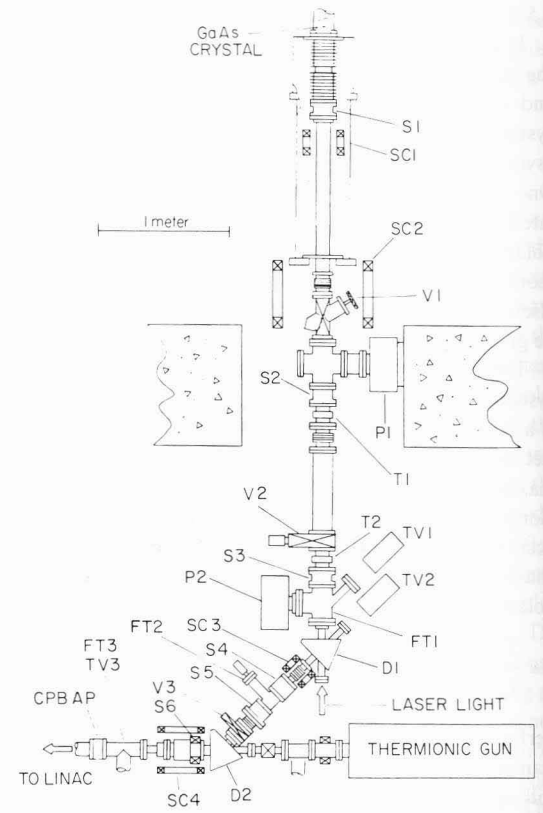

Fig. 11. The polarized electron injector beam line showing six solenoid lenses (S1–S6), two toroids (T1 and T2), the dipoles (*D1 and D2*), steering coils (*SC1–SC4*), three valves (*V1*–V3), two ion pumps (P1 and P2), three flip targets (FT1–FT3), three TV cameras (TV1–TV3), and the location of a small aperture in the chopper prebuncher (CPB AP).

The solenoidal beam-line magnetic lenses, shown in fig. 11, total six in number with five of them using iron cores. Downstream of the third solenoid is a dipole magnet, which bends the beam by 45°. A second dipole bends the beam through another 45° into a horizontal line. Following the first dipole are the fourth and fifth solenoids which together with the two dipoles form an achromatic doublet. The band pass of the achromat is 1% in momentum. The sixth solenoid, following immediately after the second dipole, focuses the beam to a waist at an aperture in the chopper–prebuncher assembly.

The beam current is monitored by toroidal current transformers [58] that are capable of providing a calibrated measure of the charge present in each beam pulse. Interfaced through an appropriate amplifier, they

* Laser Optics, substrate part #110-25220 (l/10 flatness specification and a 20–10 scratch and dig specification for surface quality). Coating type LH-41.

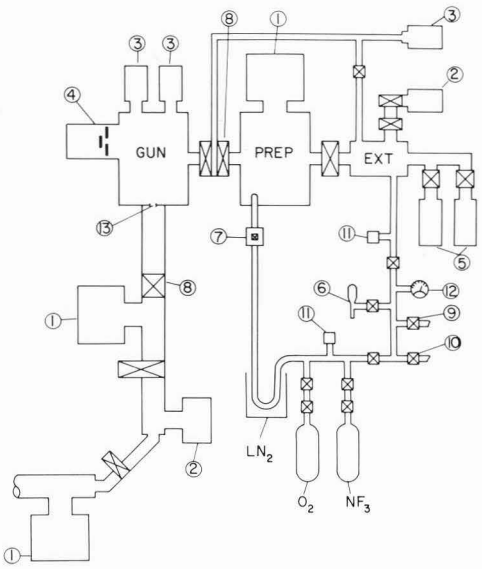

Fig. 12. A schematic of the vacuum system. Eight ion pumps are shown. Three 220 l/s ion pumps (1), two 140 l/s ion pumps (2), and three 20 l/s ion pumps (3). Other pumps that are shown include a titanium sublimation pump (4), sorption pumps (5), and a venturi pump (6). Numerous valves are indicated, including a Granville–Phillips leak valve (7), two hard seat valves (8), an overpressure valve (9), and a valve used for back-filling (10). Two thermocouple gauges (11) and a mechanical pressure gauge (12) are shown. Also indicated is a 1 cm aperture at the base of the gun chamber that facilitates differential pumping.

provide an output signal that is proportional to beam current. During tune-up (at low average current), beam position and focusing are monitored with beryllium oxide (BeO) "flip-in" targets which facilitate the adjustment of focusing and steering elements. They are viewed remotely using video cameras, and are removed from the beam path prior to full intensity operation. The locations of the toroids and the flip targets are shown in fig. 11.

4.7. The vacuum system and bakeouts

Fig. 12 contains a schematic diagram of the vacuum system including the connection between the source and the accelerator. For purposes of discussion, the vacuum system may be considered to comprise four separate sections: the extractor and gas handling region, the preparation chamber, the gun chamber and upper beam line, and the lower beam line. Each of these sections, during quiescent times, is isolated from all other sections by appropriate ultrahigh vacuum valves.

The extractor region satisfies the major gas handling requirements of the polarized source. The functions performed by the extractor region include the following:

(1) Roughing the entire polarized source and the injector beam line. (Note that a valve does exist on the lower beam line for roughing purposes also.)
(b) Back-filling the entire polarized source and injector beam line.
(c) Cycling the airlock for inserting and removing crystal samples.
(d) Flushing and filling the gas lines which are used for supplying NF_3 or O_2 during crystal activations.

The extractor region is normally isolated from the rest of the system. Typical pressures are between 10^{-6} and 10^{-8} Torr. The construction of the extractor region is completely ultrahigh vacuum (UHV) compatible, save the gas manifold, which contains Swagelok and teflon gas fittings and is separated from the rest of the extractor region by a valve.

The preparation chamber is pumped by a 220 l/s ion pump * located on top of the chamber. A baffle below the pump prevents titanium and tantalum chips from falling into the chamber. The baffle reduces the effective pumping speed to about 180 l/s. The preparation chamber is connected to the extraction region by a pneumatically operated gate valve **. The valve has an all metal bonnet seal and a Viton gate seal. The preparation chamber is connected to the gun chamber by a pneumatically operated gate valve $^{+}$, which has two all metal gate seals, each of which has a small leak rate. The region between the two seals is pumped by a separate 20 l/s pump, and a roughing connection is provided to the extraction region. The gas line that is used during activations connects to the preparation chamber through a Granville Phillips Series 203 Variable Leak Valve. The vacuum in the preparation chamber is typically about 7×10^{-11} Torr as measured by a residual gas analyzer $^{++}$. The manufacturer claims that the calibration is correct to within about a factor of two.

The gun chamber is pumped by two 20 l/s ion pumps and a titanium sublimation pump §. The titanium sublimation pump is mounted in a 4 in. diameter water cooled extension of the gun chamber. An internal baffle prevents titanium from being deposited on the internal components of the gun chamber, particularly the electrode assembly. The gun chamber is separated from the upper beam line by a 1 cm aperture which allows for differential pumping of the two regions. The pressure in the gun chamber is typically about 2×10^{-10} Torr as

* Perkin Elmer model #207-0230 DI ion pump.
** Torr Vacuum model #SVB-1.53V. Note, Torr Vacuum is now reformed under the name the Innotec Group.
$^{+}$ Torr Vacuum model #SVB-1.54V.
$^{++}$ VG Gas Analysis Limited, "Masstorr" model with Faraday cup remote head.
§ Varian Model #916-0009 Mini Ti-Ball, with a Varian Model #922-0043 control unit.

measured with a residual gas analyzer *. At the low pressures that are typical in the gun chamber, it is usually sufficient to run the Ti-Ball once every few weeks for 4 min at 45 A.

Pumping in the beam line is provided by three ion pumps, as shown in fig. 11. The solenoid lenses each have an aperture of 3.5 cm, which provides some additional differential pumping. The "front end" of the accelerator has its own ion pump which provides another stage of differential pumping when the polarized beam is injected into the accelerator through the chopper collimator.

The three regions of the source that operate at pressures below 10^{-9} Torr must be baked out following exposure to atmosphere. Typical bakeout times are as follows: the preparation chamber, 3 to 4 days; the gun chamber and the upper beam line, 5 to 7 days; and the lower beam line, 5 to 7 days. We note, however, that when baking the gun chamber and upper beam line, the disassembly and reassembly associated with the high voltage systems adds one to two weeks of work. An extensive system of heating tapes and thermocouples is needed for adequate heating and temperature monitoring. During bakeouts, insulation is provided by multiple layers of aluminum foil, although occasionally, where heat loss is a big problem, blankets fabricated of Al_2O_3 wool sandwiched in aluminum foil were used. Typical bakeout temperatures are 230 °C in the gun and preparation chambers, and about 120–150 °C in the beamline.

5. Møller polarimetry

5.1. Theoretical background

The polarization of the electron beam is determined by relativistic electron–electron (Møller) scattering [59]. Originally built for use in the Parity experiment, the Møller polarimeter is a single arm device, designed to operate at an energy of 250 MeV. In such a polarimeter, the longitudinally polarized electron beam is scattered from longitudinally polarized target electrons [60]. An asymmetry between the scattering cross sections for electrons whose spins are parallel or antiparallel provides the measure of the polarization of the incident beam. The polarized target electrons are readily obtained through the use of a ferromagnetic foil that is magnetized to saturation in an external field.

The QED treatment of relativistic electron–electron scattering, first given by Møller [59], is well understood theoretically and consequently provides an unambiguous method of electron polarimetry [61–64]. In fact, for the energy and kinematic conditions applicable at Bates, the spin-dependent asymmetry is well approximated by the ultrarelativistic first order theory that results from one-photon exchange. Based upon such an approximation, the center of mass cross section $(d\sigma/d\Omega)_{cm}$ can be expressed as [65]

$$\frac{d\sigma}{d\Omega} = \frac{\alpha^2}{8E^2}\left\{\frac{2(3+\cos^2\Theta)^2}{\sin^4\Theta} + h_1 h_2\left(\frac{2(7+\cos^2\Theta)}{\sin^2\Theta}\right)\right\}, \tag{14}$$

where α is the dimensionless fine structure constant, Θ is the cm scattering angle, and h_1 and h_2 are the helicities of the two electrons involved in the scattering process. With the longitudinal polarization of the electron beam denoted by P_L, and the longitudinal polarization of the target electrons denoted by P_{TL}, the measured Møller asymmetry, $\Delta_M(\Theta)$, can be expressed as

$$\Delta_M(\Theta) = A_M(\Theta) P_{TL} P_L, \tag{15}$$

where the physical asymmetry A_M is given by

$$A_M = \frac{d\sigma_{\uparrow\uparrow} - d\sigma_{\uparrow\downarrow}}{d\sigma_{\uparrow\uparrow} + d\sigma_{\uparrow\downarrow}} = \frac{\sin^2\Theta(7+\cos^2\Theta)}{(3+\cos^2\Theta)^2}. \tag{16}$$

The asymmetry A_M achieves a maximum value of 7/9 where $\Theta = 90°$. The result for A_M in terms of laboratory coordinates can be found from eq. (14) with the introduction of a parameter Y defined by

$$Y \equiv \frac{E_{lab}}{E'_{lab}} - 1 = \tan^2\left(\frac{\Theta}{2}\right), \tag{17}$$

where E_{lab} and E'_{lab} are the incident and scattered laboratory energies respectively. Since Møller scattering is an elastic process, two body kinematics must be satisfied, and Y bears a simple relationship to the scattering angle in the lab frame, θ:

$$Y = \frac{2E_{lab}}{m}\sin^2\left(\frac{\theta}{2}\right), \tag{18}$$

m being the rest mass of the electron. (It should be noted that when $\Theta = 90°$, $Y = 1$ and consequently $\theta = 3.66°$ at an energy $E_{lab} = 250$ MeV.) With the use of the relation

$$\frac{d\Omega_{cm}}{d\Omega_{lab}} = \frac{2E_{lab}}{m}\frac{1}{(1+Y)^2}, \tag{19}$$

the differential cross section in the laboratory frame can be written as

$$\frac{d\sigma}{d\Omega_{lab}} = \frac{\alpha^2}{4mE}\left\{\frac{(1+Y)^4+1+Y^4}{Y^2(1+Y)^2} + h_1 h_2\left[\frac{4Y^2+6Y+4}{Y(1+Y)^2}\right]\right\}, \tag{20}$$

* VG Gas Analysis Limited, "Masstorr" model with Faraday cup remote head.

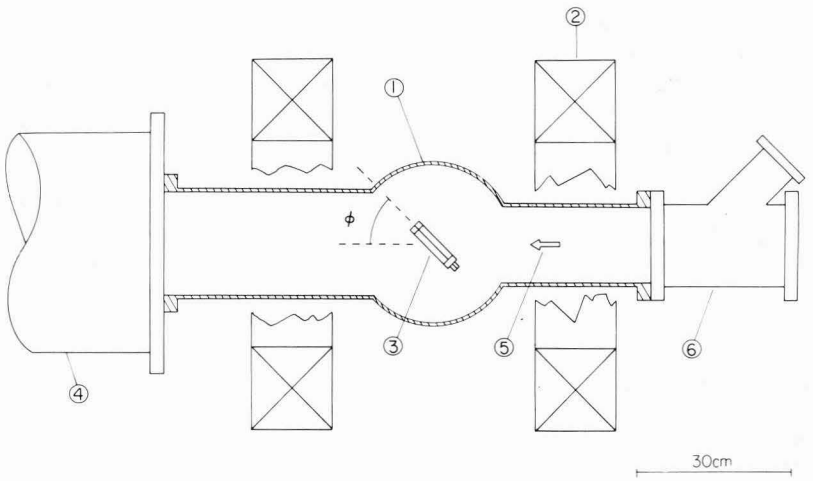

Fig. 13. A scale cross section of the Møller target chamber showing the vacuum chamber (1), the Helmholtz coils (2), the target and target ladder (3), the drift chamber leading to the tungsten collimating slits (4), the direction of the electron beam (5), and a chamber containing a BeO screen that is used for viewing the beam (6).

and the Møller asymmetry becomes

$$A_M(Y) = \frac{Y(2+3Y+2Y^2)}{(Y^2+Y+1)^2}, \tag{21}$$

an expression that is valid in either the laboratory frame or the center of mass frame.

5.2. *The Bates Møller polarimeter*

The Møller target chamber, containing a Supermendur ferromagnetic target foil and surrounded by Helmholtz coils that induce a magnetic field parallel or antiparallel to the direction of the electron beam, is shown in fig. 13. The foil is mounted on a target ladder that can be moved into or out of the beam as needed. Immediately upstream of the target chamber is another small chamber containing a beryllium oxide (BeO) screen that can also be moved into the beam for tuning purposes.

The target foil, oriented at an angle ϕ with respect to the beam axis is magnetized to saturation when a magnetic field of ~ 500 G is applied by the Helmholtz coils. Since the magnetization is constrained to lie in the plane of the foil, the longitudinal component of the target polarization P_T, is given by

$$P_{TL} = P_T \cos(\phi), \tag{22}$$

which obviously achieves a maximum value for $\phi = 0°$, an angle that is quite impossible from scattering considerations. For the measurements reported in this paper an angle of $\phi = 54.25°$ was actually used.

The target polarization P_T is measured using the same technique that was employed in earlier Møller work [60]. More details of the apparatus used in this measurement can be found in ref. [66]. The target foil is first inserted in a tightly fitting pickup coil, and the assembly is then placed in a magnetic field such that the direction of the field is normal to the windings of the pickup coil and in the plane of the target foil. The assembly is then rotated through 180°, and the changing magnetic flux through the coil induces an EMF. The target foil is then removed and the measurement is repeated, the area of the pickup coil being maintained as a constant by the substitution of a nonferromagnetic foil (such as aluminum) of the same thickness as the target foil. The difference between the two measure-

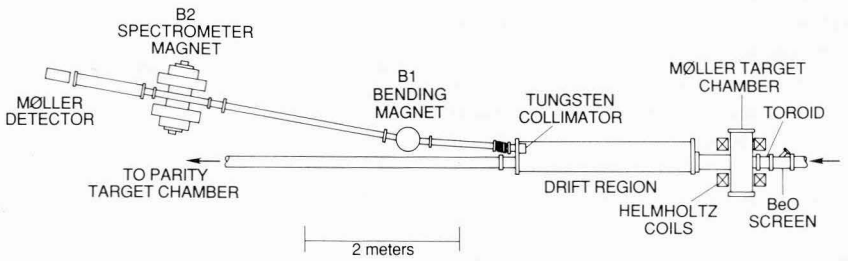

Fig. 14. Schematic of Møller polarimeter.

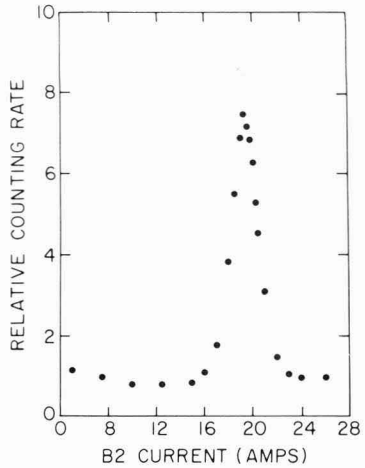

Fig. 15. The electron energy spectrum near the Møller peak as measured with the Møller spectrometer. Each point is the maximum counter value obtained during a scan of the B1 bending magnet while the B2 spectrometer magnet was held at a fixed current [64].

ments provides a measure of the magnetization of the foil.

The value of the target polarization that was used in interpreting the results of the electron beam polarization measurement is 0.084 ± 0.002. This represents the average of the two foil samples. The result is consistent with the aforementioned ealier work [60]. The two foil samples were taken from the same piece of Supermendur from which the actual Møller target foil was taken.

The Møller spectrometer shown in fig. 14 uses two magnets for energy analysis. The beam, scattered by 3.66° in the laboratory frame, is collimated by a set of vertical and horizontal tungsten slits at the end of a drift region following the Møller target chamber. The tungsten collimator presents the beam with a 1 cm by 1 cm hole. Shortly downstream of the collimator, a bending magnet (B1) bends the beam in the horizontal plane by approximately 6.5°, resulting in an angle between the scattered beam and the primary beam of about 10.2°. A second magnet, labeled spectrometer magnet (B2) in fig. 14, then bends the beam vertically down by 34°, where it is detected by a single Cherenkov counter.

The program TRANSPORT [67] was used in the design of the spectrometer, and a description of this work has been given elsewhere [66]. In brief, the spectrometer magnets provide a focus at the location of the detector with the focal plane rotated about the central trajectory by −39°. For the spectrometer tuned to an energy of 125 MeV there is a calculated energy dispersion of 1.02 cm/%. When tuned for this energy, the field in B1 is 2.74 kG and the field in B2 is 8.5 kG.

The Cherenkov counter consists of a slab of UVT lucite, 1 cm × 3 cm in cross section, bonded directly to an RCA 6810A photomultiplier tube. The counter is mounted behind a 2 cm × 4 cm aperture, formed by a 5 cm thick lead collimator. The 2 cm opening in the lead collimator, rotated by −39° in the focal plane, lies in the energy-dispersion direction. Thus, the energy resolution is 2 cm/(1.02 cm/%) = ~ 2%, a level consistent with the limitations already imposed by the effects of multiple scattering in the target.

The spectrometer is tuned to a specific energy by appropriate settings on both B1 and B2. In practice, one of the magnets is set at a fixed value while the other is scanned. From a set of scans an energy spectrum can thus be determined, as is shown in fig. 15, which shows data from extensive studies that were performed with unpolarized electrons [66]. During a polarization measurement, the magnets are are tuned to the Møller peak.

6. Performance data

6.1. Quantum efficiency

As was mentioned in section 2.1, the limited power of the cw laser and the need for relatively high peak currents makes the maintenance of high quantum efficiencies an absolute necessity. Although our objective has focused on the practical goal of building a source that could fulfill our immediate needs, rather than on the study of the subtleties of the crystal activation process itself, we believe that the experience we gained from the activation of several hundred photocathodes warrants discussion.

The two most important factors influencing quantum efficiency include the substrate from which the crystal is cut and the frequency of light used in the activation process. The first point is illustrated in table 3, which shows the average quantum efficiency, as measured with a HeNe laser, for the best and worst crystals of three different batches of GaAs substrate. A clear correlation is seen between quantum efficiency and the batch of GaAs from which the crystal originated. The tests summarized in table 3 are also separated according to the oxidizing gas used during activation. Our data are

Table 3
Quantum efficiencies in the preparation chamber

Batch #	Number of crystals tested	Oxidizing gas	Average QE [%] (# of tests)	
			Best crystal	Worst crystal
1	9	O_2	5.2 (1)	1.9 ± 0.6 (3)
2	2	O_2	10.0 ± 1.2 (6)	10.0 ± 0.8 (2)
2	2	NF_3	10.8 ± 0.6 (3)	9.8 ± 1.5 (5)
3	1	O_2	7.6 ± 0.8 (4)	
3	6	NF_3	12.1 ± 2.2 (2)	7.3 (1)

Table 4
Effect of activation light wavelength

Activation light	IR	White
No. of points	10	3
$\langle QE_{HeNe} \rangle$	8.14 ±1.72	11.27 ±2.41
$\langle QE_{IR} \rangle$	3.17 ±0.6	1.45 ±0.75
$\langle QE_{IR}/QE_{HeNe} \rangle$	0.398±0.042	0.168±0.070

consistent with some enhancement of the quantum efficiency due to using NF_3 as the oxidizing gas during the activation. The other important factor, the frequency of light used in the activation, is illustrated in table 4. During activations, three different sources of light were used for monitoring photoemission: white light, white light with a filter * that blocked wavelengths below the near-infrared, and a HeNe laser. Crystals that were activated with white light had good quantum efficiencies as measured with a HeNe laser but poor quantum efficiencies as measured with the Kr^+ laser. When crystals were activated using white light with an infrared filter, however, the quantum efficiencies were lower at the HeNe wavelength, but higher at the important near infrared lines of the Kr^+ laser. The averages of the ratios of infrared quantum efficiency to HeNe quantum efficiency are shown at the bottom of table 4. It is clear that the frequency of light used during activation has a dramatic influence on the ultimate quantum efficiency obtained during production of polarized electrons.

6.2. *Low current crystal current lifetime tests*

We studied the photocurrent lifetimes, or e-folding times, of crystals at low currents as a means of establishing baseline performance prior to high current operation. Factors of primary importance in these studies included the vacuum quality and the ambient level of cesium in the vacuum chamber. Following a suggestion of Sinclair [68], we also investigated the effectiveness of NF_3 as an oxidizing agent during the activation process.

6.2.1. *Vacuum*

Vacuum conditions are critical to the stability of the delicate surface chemistry that exists on the GaAs photocathode. Not surprisingly, the constituents of the residual gas are also critical. Using a commercial mass spectrometer, we have determined the residual gas to be mostly H_2, with smaller quantities of CO, helium, and other noble gases, dominantly argon.

The H_2 does not seem to have a particularly adverse effect on the lifetime, and at the levels present, the correlation with CO was also not noticeable. We note, however, that other workers in the field have observed [68] that both CO and CO_2 can limit lifetimes when present at sufficiently high levels. The presence of He has little effect on lifetimes: at a partial pressure of nearly 10^{-9} Torr of He, we observe lifetimes of hundreds of hours. By comparison, a similar partial pressure of air reduces the lifetime to several hours.

On the practical side, the sensitivity of crystal performance to vacuum quality means several things: the system must be carefully cleaned and well baked; vacuum bursts such as those due to sparks must be avoided; outgassing of the vacuum chamber due to accidental heating must be prevented. The last point has particular relevance for accelerator applications where magnetic lenses are frequently mounted directly on the beam pipe, thereby causing the beam pipe to outgas when the lenses are operated at relatively high current.

6.2.2. *Chamber history, the cesium seasoning effect*

Many groups have observed that it takes several activations to establish good lifetimes after a system has been open to air. It has been suggested that the presence of cesium in the chamber plays a critical role in establishing an environment that is conductive to long lifetimes [52]. Since our source comprises a multichamber system, we were in a unique position to study this effect, by contrast to most other groups who activate their crystals and use them in the same chamber. With our multichamber system, a freshly activated crystal can be moved directly into the gun chamber for a lifetime measurement before the gun chamber has ever been exposed to cesium. By successive introduction of metered amounts of cesium into the gun chamber, and by measurement of lifetimes of freshly activated crystals at each step, it is possible to see a clear reproducible increase in lifetime from several hours to hundreds of hours as the ambient level of cesium increases.

We carried out sets of tests in which we measured crystal lifetimes in the gun chamber after the gun chamber had been open to air and subsequently baked. In each set of tests, we studied the crystal lifetime as a function of the amount of cesium that had been introduced into the chamber and observed a clear dependence of the lifetime on the level of cesiation of the chamber. Two such sets of tests are summarized in fig. 16, in which the measured lifetime of a crystal is plotted as a function of the ambient cesium level in the gun chamber. We consider first the measurements taken between Oct. and Nov. of 1985, using NF_3 as the oxidizing gas during activations. The first three data points show a marked increase in lifetime as the cesium level is increased. At this point in our test, a small leak developed in the gun chamber, reducing crystal lifetimes to several hours. Rather than opening the system to fix the leak, we flushed the the leak with He, following which our mass spectrometer indicated a partial pres-

* Oriel model #51540 with 60% transmission at 750 nm.

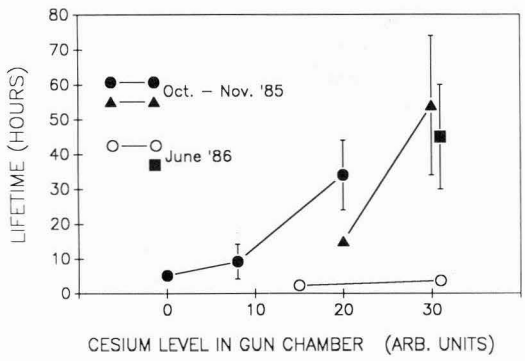

Fig. 16. Measurements of low current crystal lifetimes are shown as a function of the amount of cesium that has been deposited in the gun chamber. Two sets of data are presented from the indicated time periods. The solid points indicate crystals activated with NF_3, and the open points indicate crystals activated with O_2. With regards to the 1985 data, the solid circles indicate measurements taken prior to a small leak occurring in the gun chamber, and the solid triangles indicate measurements taken after the leak was flushed with helium. Some degradation of the gun chamber performance is evident as a result of the leak, but additional cesium quickly restored performance. With regards to the 1986 data, the performance of crystals that were activated with O_2 (open circles) are seen to differ markedly from the performance of crystals activated with NF_3 (solid square). The arbitrary units actually refers to the number of minutes during which 6 amperes had been run through a Cs dispenser.

sure of He between $(5–10)\times 10^{-10}$ Torr. With this configuration, and no further deposition of Cs, the next data point was measured, indicating that the effect of the Cs had been partially neutralized. With the introduction of additional cesium, however, the crystal lifetime more than recovered from the effects of the leak. These tests gave us a rough calibration of the amount of cesium that is required to achieve good lifetimes. One "unit" as shown in fig. 16 represents running our dispenser at 6 A for one minute. We typically would run the dispenser for 5–10 min each time we deposited cesium. They also clearly demonstrated that He, at pressures up to about 10^{-9} Torr, does not strongly affect photocathode lifetimes.

We have considered two hypotheses regarding the mechanism through which the Cs enhances the lifetimes. One is that the Cs acts as a getter for trace amounts of particularly offending gases. Although there is a titanium sublimation pump attached to the gun chamber, Cs may well be a more effective getter than titanium for the particular gases that degrade the crystal performance. One piece of evidence supporting this hypothesis is that the Cs effect does not seem to depend on where the Cs is deposited in the chamber.

A second hypothesis is that Cs may migrate from the crystal, and the presence of Cs in the chamber is necessary for establishing an equilibrium. This hypothesis is supported by the fact that we have on occasion over cesiated the gun chamber, resulting in a phenomena whereby a crystal actually needed NF_3 or O_2 to regain maximum quantum efficiency after a gun lifetime test. For the time being these questions remain unresolved, and the technique of cesiating a chamber to enhance lifetime may be looked upon as a practical solution to a problem.

6.2.3. Oxidizing gas and lifetime

It has been suggested that NF_3 provides a more stable crystal surface than does O_2 [68]. Data supporting this suggestion are shown in fig. 16. The two open circles represent lifetime tests using O_2 as the oxidizing agent. It is clear that the corresponding lifetime measurements from the previous tests in which NF_3 was used as the oxidizing agent yielded superior results. The closed square shows the results of a lifetime measurement in which the oxidizing gas was switched back to NF_3; a dramatic increase in measured lifetime is apparent. Although the data from this comparison of oxidizing gases are limited in number, the results are consistent with Sinclair's observations. We should note, however, that the vacuum in the gun chamber during these tests was poorer than usual due to contamination downstream in the beam line. The poor vacuum may have influenced the outcome of the tests. Even so, as a result of these tests we now use only NF_3 as the oxidizing gas.

6.3. Measurements of the PITA effect

We carried out measurements of the PITA effect described in section 4.5.8 in the subsection titled Systematic Control. The phase Δ of eqs. (11) and (12) was adjusted electro-optically by adjusting the voltages on the two power supplies that powered the Pockels cell. The quantity measured in every case was A_{PITA} defined by the equation

$$A_{\mathrm{PITA}}(\Delta) = \frac{I_+ - I_-}{I_+ + I_-}, \tag{23}$$

where I_+ (I_-) is the intensity of positive (negative) helicity light arriving at the vacuum window through which the laser beam enters the vacuum system. In order to minimize the effects of laser jitter, the measured light intensity was normalized to a laser pickoff signal from upstream of the helicity reversal Pockels cell but downstream of the electro-optic shutter.

The setup of the optics table is shown in fig. 9. The laser beam was formed into pulses whose helicity was reversed in a quasirandom manner on a pulse to pulse basis just as it is in the parity experiment. The light intensity I and the laser pickoff signal were each integrated and digitized over each pulse and stored on

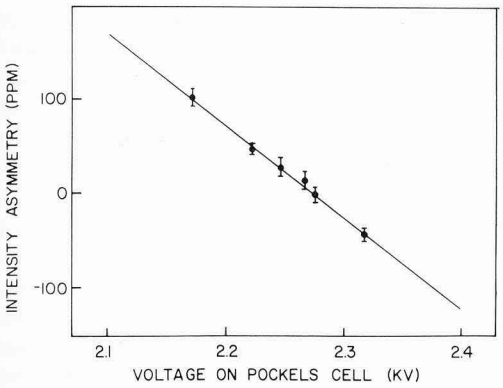

Fig. 17. A measurement of the PITA (polarization induced transport asymmetry) effect is presented. The helicity dependent asymmetry of laser light intensity is shown as a function of the positive voltage that was applied to the helicity flipping Pockels cell. The corresponding negative voltage used for each data point was chosen such that α of eqs. (11) and (12) was held fixed while Δ was varied. The light intensity was measured immediately before the vacuum window through which the laser light enters the vacuum system. A HeNe laser was used in this test.

tape. Noise generated using a digital to analog converter (DAC) was added to the integrated signal electronically and subtracted later during analysis. The asymmetries were obtained by averaging over many pulses.

The transmission of light through the laser beam transport system can be shown to have the form

$$A_{\mathrm{PITA}}(\Delta) = \frac{(\Delta - \Delta_0)\epsilon}{T} \sin(2\Theta), \qquad (24)$$

where ϵ, T and Θ can be computed from the orientation and optical properties of the mirrors. Here Δ is the phase which is controlled electro-optically, and Δ_0 is a phase that is unintentionally introduced by the various optical components. One example of a contribution to Δ_0 is the residual birefringence of the Pockels cell. In general there are other contributions as well. The stability of Δ_0 is critical for keeping A_{PITA} small. We have found that both temperature stability and the position on the Pockels cell through which the laser beam passes are important factors for keeping Δ_0 stable. As can be seen from the data shown in fig. 17, A_{PITA} depends almost linearly on Δ. During parity experiment runs, the data are analyzed online for the PITA effects so that Δ can be adjusted to keep A_{PITA} as close to zero as possible.

6.4. Operating characteristics

Table 5 summarizes the current status of various important parameters, some of which are still being improved. Below, we discuss some of the details of the measurements we have made.

6.4.1. Perveance

We determined the perveance of the gun in a series of tests in which the emitted current was measured as a function of cathode to anode voltage (see eq. (8)). The interpretation of these tests must take account of the non-uniform, approximately Gaussian distribution of laser light over the emitting surface of the crystal. As a result of the non-uniformity, a given total laser power will cause space charge saturation of the photocurrent at the central portions of the emitting surface, while the outer portions of the emitting surface, receiving less light, remain unsaturated. Consequently, for a given cathode to anode voltage, the photocurrent will not rise linearly to its saturation value, I_{SAT} (given by eq. (8)) as

Table 5
Operating characteristics

Peak current (pre-injected)	17 mA [a], 9–11 mA typical operating configuration
Average current (injected)	45–55 μA typical operating configuration
Time structure	Repetition rate 1–1000 Hz
	Pulse length 5–20 μs
Phase space	Estimated at $10^{-3}\pi mc$ cm
	(consistent with comparison with thermionic gun)
Perveance	73×10^{-6} mA/V$^{3/2}$
Beam energy	320 keV
Pulse to pulse stability	0.5–1.0%
Intrapulse stability	~ 3% jitter during 80% of pulse
Helicity correlated stability	$\sim 10^{-5}$
Lifetime	8–18 h for ~ 10 mA peak current, resulting in
	~ 5 mA accelerated peak current at 600 Hz, and ~ 50 μA average current.
	~ 30 h extrapolated lifetime (best case)
Polarization	0.36–0.40

[a] Peak current obtained with laser output power of 2.0 W, laser transport efficiency of 45%, multiline operation in the near-IR, quantum efficiencies measured as 10% with HeNe in preparation chamber, and 4% with Kr^+ laser in gun chamber, and cathode to anode voltage of 10 kV, operating without a molybdenum mask.

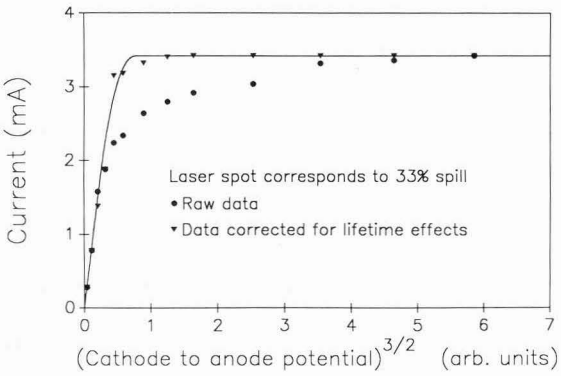

Fig. 18. A representative measurement of the perveance of the polarized electron gun. Extracted beam current is shown as a function of the cathode to anode potential raised to the 3/2 power. The extracted beam current is space charge limited toward lower voltages, and is limited by laser power and quantum efficiency toward higher voltages. The effects of a Gaussian laser spot are taken into account in the model shown with the solid line. The model is fit to the maximum observed current, the perveance, and the size of the Gaussian beam spot. A spot size corresponding to a 33% spill gave a good fit to the data. This is in reasonable agreement with the measured spot size.

a function of the incident light intensity. For incident light characterized by a Gaussian profile centered on the crystal, the total photocurrent, I_{CSAT}, at which saturation occurs at the center of the crystal, can be shown to be given by

$$I_{CSAT} = -\frac{KV^{3/2}}{\ln(S)}\left[1 - \exp\left(\frac{\ln(S)}{2}\right)\right], \qquad (25)$$

where V is the cathode to anode voltage, and S is the fraction of the Gaussian that "spills" beyond the radius of the crystal.

We carried out measurements of the perveance of the gun with several different laser spot sizes (or spills) and found that they all yielded values of K approximately 73×10^{-6} mA/V$^{3/2}$. Fig. 18 displays a representative measurement in which the photocurrent I_{SAT} (in mA) is plotted as a function of $V^{3/2}$ (in arbitrary units). In the low voltage region, the photocurrent corresponds to the saturation current I_{SAT}. The data are plotted both with and without corrections for lifetime effects (degradation of the cathode performance during the test). Some of these corrections are substantial, because at higher current, and the low electrode voltages used in these tests, the quality of the extracted beam degrades, resulting in beam-scraping and consequent outgassing of surface near the crystal. As can be seen from fig. 18, the photocurrent reaches a plateau at higher voltages, reflecting the limit determined by the available laser power and the quantum efficiency of the crystal. At lower voltages, the data were fit with a simple model that considered as free parameters the perveance, the laser beam spot size (spill), and the maximum current that would result from an arbitrarily high cathode to anode voltage.

The measured value of K predicts that for sufficiently high light intensities, 73 mA of extracted current (I_{SAT}) could be obtained at a cathode to anode voltage of 10 kV. However, eq. (25) demonstrates that for a 10% spill ($S = 0.1$), the extracted current already begins to display nonlinearities with respect to the incident light intensity at a value of I_{CSAT} of 22 mA. These results apply to an unmasked 8 mm-diameter crystal; for masks which restrict the effective crystal diameter, the currents are appreciably lower.

While the value of I_{SAT} is adequate for the parity studies, we were led to investigate how small changes in the electrode geometry might affect the perveance. From the design standpoint, at least, we discovered that small alterations in the geometry could indeed have substantial effects and in principle could have provided higher current performance. In conjunction with one of these studies we also developed an electrode geometry which would provide for in-line cesiation, thereby leading to potentially enhanced crystal lifetimes [52].

6.4.2. High current lifetimes

The lifetime of a crystal in a running configuration for the parity experiment is typically 8–18 h, and as high as 30 h, as indicated in table 5. The crystal lifetimes are very sensitive to vacuum, and better performance results when the vacuum is good. Also, at high currents, the lifetime performance is extremely sensitive to the scraping of small quantities of electron beams on metal surfaces near the gun chamber. (For example, with a loss of less than 1% of the current, less loss than we are able to resolve, the lifetime of the crystal can fall to less than one hour.) This problem has been reduced by limiting the emitting surface of the crystal through the use of an annular molybdenum mask, placed directly in contact with the GaAs crystal. The mask prevents electron emission from the perimeter of the crystal, thereby eliminating the beam halo that results from excessively strong focusing of extreme rays. Although the mask thus limits beam scraping, it also creates a condition under which the smaller emitting surface presented by the mask limits the maximum obtainable peak current.

6.4.3. Peak current

The peak current listed in table 5 is 17 mA. As the table indicates, however, we were only able to achieve this current with full laser power, and for an unmasked crystal with a quantum efficiency of 4% at 752 nm, with a cathode to anode voltage of 10 kV. Normally, however, we employ a cathode mask in order to enhance the lifetime, which results in a maximum peak current of ~ 15 mA. Typical peak currents are in the range of

9–11 mA, which results in 4.5–5.5 mA peak accelerated current, and 45–55 μA averaged accelerated current. We note that losses suffered during injection are lower than those normally quoted for the Bates Accelerator, since the chopper capture phase was expanded from 120° to 180° for polarized beam handling. (The injector of the Bates Accelerator is described in ref. [44].)

6.4.4. Injection and phase space

We have not made a direct measurement of the polarized electron gun phase space. We have found, however, that when the accelerator is tuned for the conditions of the thermionic gun very little additional tuning, if any, is needed to accelerate the polarized beam through the linac. Together with our low injection losses, this observation suggests that the transverse phase space of the polarized beam is no greater than that of the thermionic beam, a conclusion that is consistent with the computer simulations described in section 4.3.1. We note that as a result of expanding the capture fraction as described in section 6.4.3, the beam suffers an increase in the longitudinal phase space which is manifested as a degraded energy spectrum of the accelerated beam. This is not a problem for the parity experiment.

6.5. Polarization measurement utilizing Møller scattering at 250 MeV

The two primary signals used in the Møller polarization measurement are obtained from a Cherenkov counter located at the rear of the Møller spectrometer and a toroid located immediately upstream of the Møller scattering chamber. The ratio of these two signals provides a relative measure of the cross section.

During a measurement data were acquired at a rate of 60 Hz. Every 13 pulses, the signal to the gun was blanked, and pedestal data were recorded. The pedestals represent the integrated values that appear in the ADCs when the electron beam is off. For purposes of analysis, the most recent pedestal was subtracted from each signal, thus providing each signal with a zero reference point. Pedestals that were taken during positive helicity pulses were treated identically to those taken during negative helicity pulses, an approach that allows for smaller errors, since with this procedure the ADCs effectively are "zeroed" more often. (The procedure requires the assumption, however, that the pedestals do not display helicity dependent asymmetries. This assumption was justified by studies prior to the Møller measurement.) The helicity of the pulses was chosen quasirandomly using a software algorithm.

The first polarization measurement of the Bates source consisted of a series of 10 runs. As a check that the observed asymmetry was indeed due to Møller scattering, we twice reversed the polarity of the helmholtz coils that polarize the target foil. The polarization asymmetry should change sign under this reversal. The results of the ten runs are given in table 6, and are graphed in fig. 19.

Table 6
Summary of polarization measurements of June 27, 1986

Polarity of target magnet	Asymmetry [ppm]	Statistical error
+	[−6337]	[3466]
+	+13997	1753
+	+8333	2844
−	−11353	2980
−	−11193	1322
−	−12632	1278
+	+14212	1206
+	+13258	1022
+	+11455	1154
+	+10574	4974
Average Δ_M	12551	489

χ^2/deg. freedom = 760/8 = 0.95

In all but the first run, the sign of the asymmetry agreed with expectations given the magnet polarity. In light of the uncertainties of the state of our hardware during this run and in consideration of the five standard deviation discrepancy with the average value, we have eliminated this run from the data set.

The raw asymmetry, Δ_M, can be used to calculate the polarization P_e, with the aid of the formula

$$P_e = \frac{\Delta_M}{\frac{7}{9} f_{pol} P_T \cos(\phi)}, \tag{26}$$

which follows from eqs. (15) and (22) with $A_M = 7/9$ and where again P_T is the polarization of the target electrons, and ϕ is the inclination of the foil. The quantity f_{pol} is the fraction of events collected directly

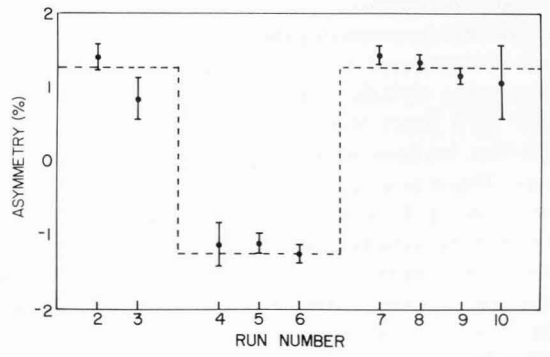

Fig. 19. The raw Møller asymmetry Δ_M of equation 28 is plotted for each of nine runs used in a polarization measurement. Also shown with the dotted line is the weighted average of the runs, with the sign adjusted to account for the target magnet polarity.

Table 7
Determination of the polarization

Quantity	Percent error contributed to final result
$\Delta_M = 1.255 \times 10^{-2} \pm 0.049$	4.0%
$P_T = 0.084 \pm 0.002$	2.4%
$\theta_T = 54.3 \pm 0.5°$	1.2%
$f_{pol} = 0.91 \pm 0.17$	1.8%
Polarization $= 0.36 \pm 0.034$	9.4% of itself

attributable to Møller scattering and accounts for the unpolarized background that is accepted by the Møller spectrometer.

We estimated the value of f_{pol} by studying the energy spectrum that is shown in fig. 15. The high energy side of the Møller peak displays a slowly rising background, while the low energy side of the peak displays a valley. We can estimate the background with a line drawn from the valley up to the background at the high energy side of the peak. At the energy of the peak, this background represents about 10% of the total signal. The background is probably composed largely of the radiative tail of electrons scattering from the iron and cobalt nuclei. Table 7 summarizes the different quantities that enter into the polarization determination.

Subsequent polarization measurements have been made on several occasions, and have yielded polarizations as high as 0.40 ± 0.03.

7. Conclusion

The source we have constructed is significantly different from all previous GaAs based polarized electron sources. Its unique multichamber design has allowed us to study performance characteristics such as crystal lifetime and quantum efficiency in controlled tests. We have demonstrated new techniques for handling and transporting crystals in an ultrahigh vacuum environment. As a result of careful optimization of quantum efficiency, we have achieved 50 μA average current on target. This was accomplished with about 10 mA peak current out of the source, ~ 1% duty factor, and nearly 50% injection efficiency into the accelerator. Our measured polarizations are ~ 36% as measured with Møller scattering. In terms of the combined operating parameters of average current and quantum efficiency, the source has met our expectations, and moreover, has exceeded the corresponding performance characteristics achieved in other reported GaAs polarized electron work. As indicated in table 5, the cathode lifetime was 8–18 h depending upon conditions. The best extrapolated lifetime was ~ 30 h during which excellent vacuum conditions prevailed.

As part of our source effort, we made important advances in the control of helicity dependent systematic effects, the most important of which was a helicity dependent asymmetry in the electron beam intensity (described in the text as the PITA effect). We made substantial progress in learning to control this effect, and typically were able to limit the size of the systematic asymmetry to the level of about 10 ppm level during a 15 min run. With the use of a manual feedback technique, preliminary results indicate that the effect remains below 1 ppm, when averaged over many runs. This fine level of control is an important milestone in our efforts to observe parity violation.

In summary, the polarized source has been successfully employed in several preliminary runs of the parity violation experiment, with efforts focusing on the study of systematic effects. The result of our most recent run indicate that systematic effects in the parity violation experiment are now controlled at our present statistical limit of 0.8 ppm, a value which is already comparable to the parity violating asymmetry predicted by the standard model. In conclusion, we point out that our work has not only advanced the techniques needed for precision measurement of parity nonconservation, but has also led to significant improvements in the understanding and operation of GaAs polarized electron sources.

Acknowledgements

We would like to acknowledge the assistance of Ann Barber, John Glossen, Matt Goodman and Scott Patch on various aspects of this work. We would also like to acknowledge G. Lampel, D.T. Pierce, R.J. Celotta, A.B. McDonald, E. Reichert, and C.K. Sinclair for useful discussions. This work was supported by the US Department of Energy under grant numbers DE-FG02-84ER40243 (Yale Univ.), DE-FG02-84ER40146 (Syracuse Univ.), DE FG02-86-ER40304 (CCNY), DE-FG02-86-ER40276 (Harvard Univ.), and contract number DE-AC02-76ER03069 (MIT Bates Linear Accelerator Center). One of us (G.D.C.) would also like to acknowledge the support of the US Air Force Office of Scientific Research under Grant no. 88-0165 (Princeton Univ.).

References

[1] E. Garwin, D.T. Pierce and H.C. Siegmann, Helv. Phys. Acta 47 (1974) 343.
[2] G. Lampel and C. Weisbuch, Sol. Stat. Commun. 16 (1975) 877.

[3] D.T. Pierce and F. Meier, Phys. Rev. B13 (1976) 5484.
[4] C.K. Sinclair, E.L. Garwin, R.H. Miller and C.Y. Prescott, AIP Conf. Proc. 35 (1976) 424.
[5] D.T. Pierce, R.J. Celotta, G.-C. Wang, W.N. Unrtl, A. Galejs, C.E. Kuyatt and S.R. Mielczarek, Rev. Sci. Instr. 51 (1980) 478.
[6] C.K. Sinclair, in: High-Energy Physics with Polarized Beams and Polarized Targets, eds. C. Joseph and J. Soffer (Birkhäuser, Basel, 1981) p. 27.
[7] M.J. Alguard et al., Phys. Rev. Lett. 37 (1976) 1258.
[8] M.J. Alguard et al., Phys. Rev. Lett. 37 (1976) 1261.
[9] M.J. Alguard et al., Phys. Rev. Lett. 41 (1976) 70.
[10] C.Y. Prescott et al., Phys. Lett. B77 (1978) 347.
[11] C.Y. Prescott et al., Phys. Lett. B84 (1979) 524.
[12] R.G. Arnold, C.E. Carlson and F. Gross, Phys. Rev. C23 (1981) 263.
[13] R. Madey et al., Bates Proposal #85-05.
[14] R. Milner et al., Bates Proposal #88-02 (1988).
[15] A. Bernstein et al., Bates Proposal #88-10 (1988).
[16] T.W. Donnelly and I. Sick, Rev. Mod. Phys. 56 (1984) 461.
[17] C.N. Papanicolas et al., Bates Proposal 87-03 (1987).
[18] O'Connell et al., Bates Proposal #87-03 (1987) unpublished.
[19] Calarco et al., Bates Proposal #86-14 (1986) unpublished.
[20] T.W. Donnelly, in: New Vistas in Electro-Nuclear Physics (Nato Advanced Study Institute, Banff, Alberta, Canada, 1985).
[21] P.A. Souder, V.W. Hughes and M.S. Lubell, Bates Proposal 77/14 (Sept. 1977) unpublished.
[22] P.A. Souder et al., in: High Energy Physics with Polarized Beams and Targets, eds. Joseph and J. Soffer (Birkhäuser Verlag, Basel, 1981) p. 454.
[23] P. Souder et al., in: High Energy Spin Physics – 1982, ed. G.M. Bunce (AIP, New York, 1983) p. 574.
[24] G. Feinberg, Phys. Rev. D12 (1975) 3575.
[25] A good summary of the characteristics of the Bates machine is given in the Bates Linear Accelerator Center Annual Scientific and Technical Report, ed. G. Nixon (MIT Bates Linear Accelerator Center, Middleton, MA, 1984).
[26] J. Kessler, Polarized Electrons, 2nd ed., Springer Series on Atoms and Plasma, vol. 1 (Springer, New York, 1985).
[27] G. Baum et al., Appl. Phys. 14 (1977) 149.
[28] E. Kisker et al., Phys. Rev. B18 (1978) 2256.
[29] W. von Drachenfels et al., Nucl. Instr. and Meth. 140 (1977) 47.
[30] T.M. Müller, Ph.D. Thesis, Bonn, IR-78-12 (1978) unpublished.
[31] P.F. Wainwright et al., Rev. Sci. Instr. 49 (1978) 571.
[32] L.G. Gray, K.W. Giberson, Chu-Cheng, R.S. Keiffer, F.B. Dunning and G.K. Walters, Rev. Sci. Instr. 54 (1983) 271.
[33] M.J. Alguard et al., Nucl. Instr. and Meth. 163 (1979) 29.
[34] W. Achenbach et al., Int. Symp. on Weak and Electromagnetic Interactions in Nuclei, (1986) to be published.
[35] E. Reichert, in: High Energy Spin Physics – 1982, ed. G.M. Bunce (AIP, New York, 1983) p. 580.
[36] A.B. McDonald et al., ibid., p. 586.
[37] E.D. Earle et al., submitted for publication in Can. J. Phys.
[38] W.E. Spicer, Phys. Rev. 112 (1958) 114.
[39] R.L. Bell and W.E. Spicer, Proc. IEEE 58 (1970) 1788.
[40] W.E. Spicer, Appl. Phys. 12 (1977) 115.
[41] C. Sinclair, private communication (1988).
[42] G. Lampel, Phys. Rev. B31 (1985) 3859 and 3872.
[43] J. Haimson, in: Linear Accelerators, eds. P.M. Lapostolle and A.L. Septier (North-Holland, Amsterdam, 1970) p. 439.
[44] J. Haimson, Particle Accelerator Conf., Chicago (1971).
[45] J.R. Pierce, Theory and Design of Electron Guns (Van Nostrand–Reinhold, Princeton, NJ, 1959).
[46] G.R. Brewer, in: Focussing of Charged Particles, ed. A. Septier (Academic Press, New York, 1967) p. 36.
[47] I. Langmuir and K.B. Blogett, Phys. Rev. 22 (1923) 347.
[48] W. Hermannsfeldt, SLAC Report 226 (Stanford Linear Accelerator Center, Stanford, CA, 1979).
[49] G. Cates and M. Lubell, The Electron Optics Design For the Bates Polarized Electron Gun, Yale University, informal internal report (1981) unpublished.
[50] H.R. Schaefer, G. Cates, R. Michaels, V.W. Hughes, M.S. Lubell and P.A. Souder, The Bates GaAs Polarized Electron Source, 1983 SLAC Workshop on Polarized electron sources (the planned proceedings were never published).
[51] M.E. Schulze et al., Modifications to the Anode-Cathode Structure of the Bates Polarized Source, internal memo, MIT Bates, Middleton MA (1987) unpublished.
[52] F.C. Tang, M.S. Lubell, K. Rubin and A. Vasilakis, Rev. Sci. Instr. 57 (1986) 3004.
[53] W.R. Bennet, Jr., Some Aspects of the Physics of Gas Lasers (Gordon and Breach, New York, 1973).
[54] A. Maitland and M.H. Dunn, Laser Physics (North-Holland, Amsterdam, 1969).
[55] E. Hecht and A. Zajac, Optics (Addison–Wesley, Reading Massachusetts, 1974).
[56] G.D. Cates, Ph.D. thesis, Yale Univ. (1987) unpublished).
[57] H. Frauenfelder and A. Rossi, in: Methods of Experimental Physics, vol. 5, part B, eds. L.C.L. Yuan and C.S. Wu (Academic Press, New York, 1963).
[58] P.C. Dunn, Nucl. Instr. and Meth. 165 (1979) 165.
[59] C. Møller, Ann. Phys. (Leipzig) 14 (1932) 531.
[60] P.S. Cooper et al., Phys. Rev. Lett. 34 (1975) 1589; P.S. Cooper, Ph.D. Thesis, Yale University (1975) unpublished.
[61] A.M. Bincer, Phys. Rev. 107 (1957) 1434.
[62] L.L. DeRaad and Y.J. Ng, Phys. Rev. D10 (1974) 683.
[63] L.L. DeRaad and Y.J. Ng, Phys. Rev. D10 (1974) 3440.
[64] L.L. DeRaad and Y.J. Ng, Phys. Rev. D11 (1975) 1586.
[65] V.B. Berestetskii, E.M. Lifshitz and L.P. Pitaevskii, Quantum Electrodynamics – Landau and Lifshitz course on Theoretical Physics, vol. 4 (Pergamon, Oxford, 1982).
[66] A.E. Barber, Masters Thesis, MIT (1980) unpublished.
[67] K.L. Brown et al., SLAC Report SLAC-91 (1974).
[68] C.K. Sinclair, private communication (1986).